Contrast Sensitivity and Spatial Frequency Response of Primate Cortical Neurons in and Around the Cytochrome Oxidase Blobs

DAVID P. EDWARDS,* KEITH P. PURPURA,*† EHUD KAPLAN*‡

The striate cortex of macaque monkeys contains an array of patches which stain heavily for the enzyme cytochrome oxidase (CO blobs). Cells inside and outside these blobs are often described as belonging to two distinct populations or streams. In order to better understand the function of the CO blobs, we measured the contrast sensitivity and spatial frequency response of single neurons in and around the CO blobs. Density profiles of each blob were assessed using a new quantitative method, and correlations of local CO density with the physiology were noted. We found that the CO density dropped off gradually with distance from blob centers: in a typical blob the CO density dropped from 75% to 25% over 100 μm. Recordings were confined to cortical layers 2/3. Most neurons in these layers have poor contrast sensitivity, similar to that of the parvocellular neurons in the lateral geniculate nucleus. However, in a small proportion of layers 2/3 neurons we found higher contrast sensitivity, similar to that of the magnocellular neurons. These neurons were found to cluster near blob centers. This finding is consistent with (indirect) parvocellular input spread uniformly throughout layers 2/3, and (indirect) magnocellular input focused on CO blobs. We also measured spatial tuning curves for both single units and multiple unit activity. In agreement with other workers we found that the optimal spatial frequencies of cells near blob centers were low (median 2.8 c/deg), while the optimal frequencies of cells in the interblob regions were spread over a wide range of spatial frequencies. The high cut-off spatial frequency of multi-unit activity increased with distance from blob centers. We found no correlation between spatial bandwidth and distance from blob centers. All measured physiological properties varied *gradually* with distance from CO blob centers. This suggests that the view of blob cells subserving visual functions which are entirely distinct from non-blob cells may have to be reevaluated.

Visual cortex   Cytochrome oxidase blobs   Primate   Spatial frequency   Contrast sensitivity   Signal detection theory

INTRODUCTION

The mammalian cortex is often viewed as a collection of modules, a regular array of similar components (see LeVay & Nelson, 1991 for a critical review). Examples of this modular structure include the ocular dominance columns and orientation selectivity columns in the visual cortex (Ungerleider & Mishkin, 1982) and the whisker barrels in the somatosensory cortex (Woolsey & van der Loos, 1970). The modular structure is thought to embody an optimization of anatomical and physiological constraints, and understanding this organization is widely believed to be crucial for the elucidation of the function of the cortex.

A distinctive feature of striate visual cortex in primates is the lattice of blobs or puffs that can be seen after staining for mitochondrial cytochrome oxidase (CO) (Wong-Riley & Carroll, 1984; Horton & Hubel, 1981; Horton, 1984; Hendrickson, Hunt & Wu, 1981). These blobs denote regions of high metabolic activity, and have been the subject of intense study since their discovery. Much of this work attempted to determine how blobs differ from their surrounding interblob regions. Blob neurons were shown to contain a larger number of darkly reactive mitochondria than were their interblob counterparts, indicating a greater concentration of CO reaction product (Wong-Riley & Carroll, 1984). Other reported biochemical differences between blobs and interblobs include the relative amounts of neuropeptide Y (Kuljis & Rakic, 1989) and parvalbumin (Blümcke, Hof, Morrison & Celio, 1990). Anatomical studies show differences in the underlying Meynert cell distribution (Fries, 1986; Payne & Peters, 1989) and capillary density (Zheng, LaMantia & Purves, 1991). Physiological

*Laboratory of Biophysics, Rockefeller University, New York, NY 10021, U.S.A.
†Department of Neurology and Neuroscience, Cornell University Medical College, New York, NY 10021, U.S.A.
‡To whom all correspondence should be addressed [*Email* kaplan@rockvax.bitnet].

studies reported that blob neurons are color-selective, non-oriented (Livingstone & Hubel, 1984; Ts'o & Gilbert, 1988), and tuned to low spatial frequencies (Silverman, Grosof, De Valois & Elfar, 1989; Born & Tootell, 1991a), whereas those in interblob regions are spectrally broad-band, oriented and tuned to high spatial frequencies. This dichotomous view of the blobs and interblob regions led to the notion that they are parts of two distinct visual streams, which segregate visual functions such as the analysis of color, motion, form etc. (Livingstone & Hubel, 1988).

The geniculate input to the visual striate cortex is comprised of two major pathways: the parvocellular pathway contains neurons from the upper four layers of the lateral geniculate nucleus, whereas the magnocellular afferents arise from neurons situated in the lower two geniculate layers. Parvocellular neurons have receptive fields which are smaller than those of magnocellular neurons (Kaplan & Shapley, 1982; Derrington & Lennie, 1984). Many parvocellular neurons are color opponent, i.e. they are excited by some wavelengths and inhibited by others, while magnocellular neurons respond with the same polarity of response to a broad range of wavelengths (Wiesel & Hubel, 1966). The luminance contrast gain of magnocellular neurons is much higher than that of parvocellular neurons (Shapley, Kaplan & Soodak, 1981; Kaplan & Shapley, 1982; Derrington & Lennie, 1984), and thus magnocellular neurons are stimulated more effectively at low contrasts than are parvocellular neurons.

It is known that the magnocellular and parvocellular pathways remain segregated up to their termination in layer 4C of striate cortex, with parvocellular afferents terminating in $4C\beta$ and magnocellular afferents terminating in $4C\alpha$ (Hubel & Wiesel, 1972; Hendrickson, Wilson & Ogren, 1978; Blasdel & Fitzpatrick, 1984). However, the nature of the magnocellular and parvocellular streams is less well defined past the thalamocortical input layers of striate cortex. For example, Blasdel, Lund and Fitzpatrick (1985) demonstrated a diffuse projection in macaque monkeys from layer $4C\beta$ into layers 2/3, while input from layer $4C\alpha$ was found to be more focused. Lachica, Beck and Casagrande (1992), using anatomical techniques, reported that in macaque monkeys blobs receive indirect magnocellular (via $4C\alpha$) and parvocellular input (via $4C\beta$), whereas interblobs receive only indirect parvocellular input. Several groups have also reported a direct input from the koniocellular or intercalated layers of the LGN to the blobs [Fitzpatrick, Itoh and Diamond (1983) in squirrel monkey, and Lachica et al. (1992) and Hendry and Yoshioka (1994) in macaques].

The influence of the magnocellular and parvocellular pathways in extrastriate cortex is unclear so far. However, studies of information flow from these pathways indicate that magnocellular signals appear to flow from layers $4C\alpha$ and 4B of striate cortex to the thick stripes of area V2, then to areas V3d and MT. Signals from the parvocellular pathway appear to flow from layers $4C\beta$ and 2/3 of striate cortex to the thin stripes and

interstripes of area V2, then to area V4 (Hubel & Wiesel, 1972; Lund, 1973; Lund & Boothe, 1975; Maunsell & Van Essen, 1983; DeYoe & Van Essen, 1985; Shipp & Zeki, 1985; Burkhalter, Felleman, Newsome & Van Essen, 1986; Ungerleider & Desimone, 1986a, b; Hubel & Livingstone, 1987). The output to extrastriate cortex is often divided into the posterior parietal and inferotemporal pathways (Ungerleider & Mishkin, 1982). The posterior parietal pathway is thought to be concerned with motion processing, and to be influenced primarily by the magnocellular stream. The inferotemporal pathway appears to subserve form vision, and it is thought to have a combination of magnocellular and parvocellular inputs (Livingstone & Hubel, 1987, 1988; Morel & Bullier, 1990; Baizer, Ungerleider & Desimone, 1991). This suggests that there must be a substantial mixing of magnocellular and parvocellular inputs at some point in the cortex. The location and manner in which the magnocellular and parvocellular pathways converge, combine, and function in layers 2/3 is therefore of considerable interest.

We have studied the luminance contrast sensitivity and spatial frequency tuning of cortical neurons, and correlated the measurements with the CO architecture in layers 2/3. This serves two purposes: (1) it aids us in piecing together the flow of information from the parvo- and magnocellular neurons to higher visual cortical centers; and (2) it will contribute to a deeper understanding of the functional significance of the CO blobs and their possible role in pattern vision.

Contrast sensitivity

The contrast gain of M retinal ganglion cells is 8 times higher than that of P retinal ganglion cells (Kaplan & Shapley, 1986). A difference in contrast sensitivity is also found between the input layers of the primary visual cortex; Hawken and Parker (1984) reported that neurons in the magnocellular input layer ($4C\alpha$) are more sensitive to contrast than those in the parvocellular input layer ($4C\beta$). Tootell, Hamilton and Switkes (1988a) reported that during stimulation with low-contrast patterns, blob regions exhibited a slightly greater uptake of 2-deoxy glucose (2-DG) than did the surrounding interblob regions, suggesting that the blobs constitute a "high contrast sensitivity" system of cells. It is possible that this increased uptake is due to higher contrast sensitivity of individual cells in the blobs. However, we cannot rule out the possibility that the blobs simply contain a higher density of active neurons than do the interblob regions. A study of the contrast dependence of single neuron responses is required to better understand the basis of these 2-DG results.

Hubel and Livingstone (1990) measured the contrast thresholds of neurons in layers 2/3. Their data show no significant difference between the average contrast thresholds of blob and interblob neurons. However, they measured contrast threshold as the contrast required to generate a half-maximal response. The variability of the response was not taken into account. As will be

illustrated in this paper, the ability of neurons to detect a stimulus is profoundly influenced by the variability of the response. Taking the variability into account provides a measure of contrast sensitivity that is more closely related to psychophysical contrast sensitivity.

Spatial frequency tuning

The second stimulus parameter we examined was spatial frequency tuning, which reflects the spatial structure and scale of receptive fields. Studies using 2-DG have shown that there is a columnar organization of spatial frequency tuning in striate cortex. In monkeys, Tootell, Silverman, Hamilton, Switkes and De Valois (1988b) found a correlation of spatial frequency tuning with the pattern of CO staining in the superficial layers of striate cortex. Gratings of high spatial frequency produced increased 2-DG uptake in interblob regions, whereas low spatial frequency stimulation showed preferential uptake in blobs.

Two studies have examined spatial frequency organization using single- and multi-unit recordings in and around the CO blobs (Silverman et al., 1989; Born & Tootell, 1991a). Both found, in confirmation of the 2-DG results, that the optimal spatial frequencies for blob cells were lower than those of interblob cells. These studies disagreed, however, on the nature of the transition from blobs to interblobs. Born and Tootell (1991a) report that the transition is abrupt at the blob "borders", but Silverman et al. (1989) found a gradual transition.

Relating the optimal spatial frequency of cortical cells to the magno/parvocellular pathways is difficult since the spatial frequency tuning of cortical cells differs significantly from that of geniculate cells: cortical cells are much more sharply tuned, and exhibit clear optimal spatial frequencies compared with the broader tuning of cells in the lateral geniculate (Maffei & Fiorentini, 1973; De Valois, De Valois, Ready & von Blanckensee, 1975; Schiller, Finlay & Volman, 1976; Movshon, Thompson & Tolhurst, 1978a; De Valois, Albrecht & Thorell, 1982a). In addition, cortical cells exhibit novel receptive field characteristics such as sharp orientation selectivity and end-stopping (Hubel & Wiesel, 1962; De Valois, Thorell & Albrecht, 1985). More importantly, it has been shown that cutoff spatial frequencies do not differ significantly between magno- and parvocellular neurons (Kaplan & Shapley, 1982; Hicks, Lee & Vidyasagar, 1983; Blakemore & Vital-Durand, 1986; Crook, Lee, Tigwell & Valberg, 1987; Kaplan, Lee & Shapley, 1990). When measured from contrast sensitivity functions, the cut-off frequency indicates the spatial resolution limit of the cell. If the spatial tuning of cells in and around the blobs is dictated by magno/parvocellular inputs, one might expect their cut-off spatial frequencies to be similar.

The responses of visual neurons to patterns are determined by their spatial transfer function, especially by the bandwidth and high frequency cut-off. Since previous studies of layers 2/3 provided no information on these parameters, we have studied them together with the optimal spatial frequency, and related the results to the CO architecture. Bandwidth determines the sharpness of tuning of the cells, and is of interest since bandwidths in the orientation and spatial frequency domains have been shown to be correlated (De Valois et al., 1982a).

METHODS

Animal preparation

We recorded single- and multi-unit activity in tangential penetrations of striate cortex of Old World monkeys (Macaca fascicularis). Anesthesia was induced with ketamine hydrochloride (Vetalar, 10 mg/kg), and was supplemented by i.v. injection of thiamylal (Surital, 2.5%) during surgery. In early experiments animals were maintained during the recording with urethane (initial loading dose of 100 mg, 20 mg/kg/hr thereafter). We used sufentanil citrate (Sufenta, 2–6 mg/kg/hr) for long-term anesthesia in later experiments. No consistent difference was noted between the responses obtained under Sufenta and those obtained under urethane. The state of anesthesia was monitored by continuous recordings of blood pressure (through an arterial cannula) and EEG. Animals were paralyzed with gallamine triethiodide (Flaxedil, 5–15 mg/kg/hr), and artificially respired (end-tidal CO_2 3.5%). Animals were given a one-time dose of i.v. dexamethasone (Decadron, 6 mg) to prevent brain edema.

Eye drops of 1% atropine sulfate solution were used to maintain cycloplegia, and the eyes were covered with gas-permeable hard contact lenses. All incisions were preceded by ample subdermal injections of Novocaine. The femoral veins were cannulated to allow administration of i.v. drugs. A urinary catheter was inserted to monitor fluid balance. Blood pressure, heart rate, end-tidal expired CO_2 and electrocardiogram were monitored continuously throughout the experiment using a Hewlett–Packard patient monitor (Model 78354A). Temperature was monitored and maintained at 38°C with a d.c. servo circuit connected to a heating pad.

Animals were fixed in a stereotaxic apparatus. The third or fourth lumbar vertebral spine was clamped to elevate the animal above the table to minimize the effect of respiratory movements on electrode recordings.

Recording

Refractive error was determined by retinoscopic examination. Refraction was also checked electrophysiologically and found to be in good agreement with the retinoscopic estimates. The retinoscope also allowed an estimate of astigmatic error, which was then corrected by cylindrical lenses. The positions of foveas and optic disks were mapped on a tangent screen 114 cm away from the eyes with a fundus camera. Refractive adjustment and eye position were checked several times during the course of the experiment.

For cortical recordings, the scalp was exposed along the mid-line, and a plate of bone approx. 1 cm^2, centered 15 mm anterior to the occipital ridge and 10 mm lateral

(Ts'o & Gilbert, 1988) was removed from the skull. A slit in the dura approx. 2 mm long was made in the sagittal direction just anterior to the posterior bank of the bone hole, and a glass-coated tungsten microelectrode, plated with platinum black (Merrill & Ainsworth, 1972) was inserted tangential to the cortical surface (usually at an angle of ~ 20 deg, with the electrode tip directed posteriorly). This configuration allowed the slender electrode to move relatively long distances (1–5 mm) through the superficial layers, and also to slip easily under the bone where the cortex is less likely to be damaged. The hole was covered with cooled agar which was in turn covered with Vaseline to prevent drying during the long tangential penetrations.

Geniculate recordings were made with saline-filled glass microelectrodes with tips of 2–4 μm and resistances of 8–25 MΩ. The electrode locations in the geniculate layers were inferred from the sequence of changes in eye dominance, from electrode depth readings, and from the latency of response to electrical stimulation of the optic chiasm.

Single units were isolated with the help of a digital oscilloscope (Nicolet Binary Digital I/O Model 206). If triggered spikes had the same amplitude and shape, and if spikes never fired at full amplitude during the refractory period, the recording was accepted as a single unit. All recordings were extracellular. The electrode position was marked from time to time with electrolytic lesions (3 pulses of 3 μA, 2 sec each).

Recordings of multiple units were made when single units could not be well isolated. Most multi-unit recordings were comprised of 2–4 units, judging qualitatively from the height and shape of individual spikes. Occasionally, multiple unit and single unit recordings were made simultaneously—each on a separate recording channel; however, most multi-unit recordings did not have corresponding single unit data.

Visual stimulation

An electronic visual stimulator developed in our laboratory displayed the visual stimuli (Milkman, Schick, Rossetto, Ratliff, Shapley & Victor, 1980). It was interfaced to a PDP 11/73 computer via a direct memory access (DMA) channel. The stimuli were displayed on a Princeton MultiSync Color Monitor (120 frames/sec) for stimulating cortical units and on a Tektronix (Beaverton, Ore.) 690SR color monitor for recordings from geniculate units, which were investigated in a separate series of experiments.

Look-up tables for the visual stimulator were created to ensure a linear relationship between the monitor input voltage and displayed luminance. These were determined by mounting a photo-diode over the monitor screen, and measuring the output luminance in response to linear ramps of voltage delivered to each CRT gun in succession. The visual stimuli were drifting black and white sine wave gratings. Contrast was defined as $(L_{max} - L_{min})/(L_{max} + L_{min}) \times 100$, where L_{max} and L_{min} are the maximum and minimum luminance of the grating.

Cell classification

Single-unit receptive fields were mapped on a tangent screen using bright or dark moving bars. Orientation preference and receptive field size were noted, as well as the presence or absence of end-stopping. After characterizing units with hand-held stimuli, further receptive field properties were determined with keypad-controlled visual stimulation. Optimal orientation, spatial frequency, temporal frequency and grating length (optimally windowed for end-stopped units) were determined by listening to the cell discharge, and by observing on-line peri-stimulus time (PST) histograms of the average responses.

Following the manual classification of units, we measured each neuron's response to an optimal size patch of drifting sine wave grating which varied in orientation, spatial and temporal frequency. Complex cells were distinguished from simple cells by examining the ratio of the mean discharge to the first harmonic amplitude (Skottun, De Valois, Grosof, Movshon, Albrecht & Bonds, 1991), with ratios > 1 indicating complex cells. Our response measure for complex cells was the mean firing rate (Spitzer & Hochstein, 1985; De Valois, Yund & Hepler, 1982b; Movshon *et al.*, 1978a,b). For simple cells and geniculate neurons we recorded the amplitude of the first Fourier component, which is the amplitude of the best-fitting sinusoid to the PST histograms at the temporal frequency of the stimulus. Responses were typically averaged over 16–24 cycles of the stimulus. Response variance (the complex variance of the response over all cycles of the stimulus) was then determined as described elsewhere (Croner, Purpura & Kaplan, 1993).

We collected orientation tuning curves using the optimal spatial frequency as determined subjectively with the keypad. Under computer control, drifting gratings (at a luminance contrast of 90%) were presented at 18 orientations in a pseudo random order, evenly covering all orientations in 20 deg steps. Optimal orientation was determined as the orientation which produced peak response.

Spatial tuning curves at the optimal orientation were measured with 11–13 spatial frequencies presented in pseudo random order. If the range of spatial frequencies was not sufficient to cover the response range of the cell, an additional series of spatial frequencies was used. Optimal spatial frequency was determined as the frequency that elicited the strongest response from the cell. For many single units exhibiting side- or end-inhibition (Hubel & Wiesel, 1965; Born & Tootell, 1991b), we measured spatial tuning curves before and after windowing of the stimulus. Cut-off spatial frequency was determined from the spatial tuning curve as the highest spatial frequency at half-maximal response. Since the spontaneous discharge differed from cell to cell, half-maximal response for complex cells was defined as the response which was half-way from spontaneous discharge to maximal response. Low cut-off spatial frequency was also measured at half-maximal response. Spatial tuning

bandwidth was determined by the spatial frequency span between the low and high cut-off spatial frequencies.

Optimal temporal frequency was then determined by presenting gratings drifting at a series of temporal frequencies at the optimal orientation and spatial frequency. Optimal window length and width were similarly determined.

Contrast sensitivity

After the optima were determined, we measured the responses of each cell to drifting gratings at a series of contrasts ranging from 0% to 96%, presented in pseudo random order at the optimal orientation, spatial frequency, temporal frequency, grating length and width. Each stimulus was presented for 4 sec, preceded by a 4-sec blank (zero contrast) run. This blank was necessary for two reasons: to allow the cell to recover from possible effects of prior stimulation, and to monitor the level of spontaneous discharge for each value of contrast. For the purposes of subsequent analysis, each cycle of the (periodic) stimulus was considered a "trial", e.g. a grating drifting at 4 Hz comprised 16 trials per 4 sec run.

The firing rate was calculated for each trial. Typically, 10–20 complete contrast series were presented to each cell.

We then applied signal detection theory (Green & Swets, 1966) to the contrast–response data, following the technique of Tolhurst, Movshon and Dean (1983), illustrated in Fig. 1. The first column shows pulse number distributions (PNDs) for a hypothetical neuron. These are determined by calculating the firing rate of the neuron for repeated presentations of a stimulus, then plotting the resulting distribution. The "noise" distributions are those collected during blank (i.e. zero contrast) trials, and the "signal + noise" distributions are those collected during non-blank (i.e. non-zero contrast) trials. Note the increasing separation between the noise and signal + noise distributions as stimulus strength increases. This is due to increasing neuronal firing rates in response to stronger stimuli. From the PNDs, receiver operator characteristic (ROC) curves are generated. Each point on the ROC curve represents a criterion firing rate, or detection threshold. The "false alarm" probability is determined by the percentage of noise
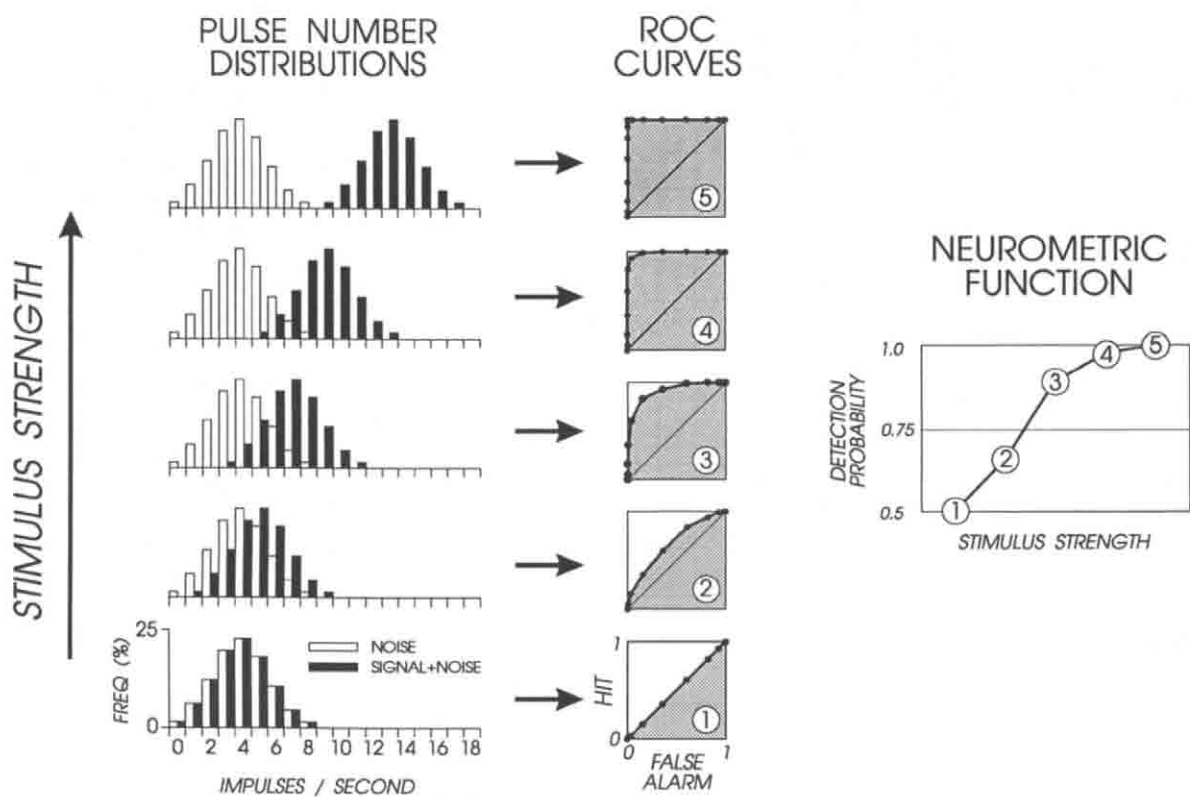

FIGURE 1. Simplified summary of ROC analysis. **Pulse number distributions:** these show the distribution of firing rates for a hypothetical neuron for many repeated trials of the stimulus. Noise distribution is collected during blank (e.g. zero contrast) trials. Signal + noise distribution is collected during trials which contain non-zero contrast stimuli. Increasing the stimulus strength increases the neuronal firing rate, and thus widens the separation between noise and signal + noise distributions. **ROC curves:** these plot the probability of a "hit" (the probability that a criterion firing rate falls within the signal + noise distribution), vs the probability of a "false alarm" (the probability that the criterion falls within the noise distribution). A "hit" indicates a "correct" response to the presentation of a stimulus. A "false alarm" indicates a response when no stimulus is presented). Each point on the ROC curve represents a different criterion firing rate. Examination of the figure reveals that the criterion firing rate increases as one moves from the top-right corner to the bottom-left corner of the figure. Integrating under the ROC curve (shaded area) gives the detection probability, or the probability that the neuron would be able to correctly choose a signal trial from a blank trial, based on its firing rate. **Neurometric function:** this plots the detection probability as a function of stimulus strength. Detection probability of 0.5 indicates "chance" performance. Detection probability of 1.0 indicates "perfect" detection, or a complete separation of noise and signal + noise distributions.

trials greater than or equal to the criterion. The "hit" probability is the percentage of signal + noise trials greater than or equal to the criterion. Integrating under the ROC curve gives the detection probability, or the probability that the neuron could correctly distinguish a signal trial from a blank trial, based on its firing rate. Plotting detection probability vs stimulus strength produces a neurometric function (Fig. 1), similar to the familiar psychometric function.

For simplicity of presentation, the variances of the noise and signal + noise distributions in Fig. 1 have been made equivalent. However, note that increasing the variance of one or both distributions will result in a *decrease* in the detection probability, since the two distributions will overlap to a greater degree.

Using ROC analysis, we determined neurometric functions for each neuron, and fit them using the hyperbolic ratio, or Michaelis–Menten equation. This function has been shown to produce the best fit to cortical contrast–response functions (Albrecht & Hamilton, 1982), and it provided a good fit to our neurometric functions as well (see Figs 2–4, and Britten, Shadlen, Newsome & Movshon, 1992). From the fitted neurometric functions we calculated the contrast threshold, which is the lowest contrast giving a detection probability of 75%. The contrast sensitivity is the reciprocal of the contrast threshold.

Histology

Following each experiment the animal was perfused through the heart after the administration of 5 cm³ of heparin and an overdose of the barbiturate Surital. The animal was flushed with 0.1 M phosphate buffer, then fixed with 4% paraformaldehyde in 0.1 M phosphate buffer.

The brain was then removed and a block of operculum containing electrode tracks was cut away from the rest of the brain. Gray matter below the opercular cortex was removed by carefully dissecting down the white matter with the blunt end of a scalpel handle. Thus isolated, the opercular cortex was inserted between two glass slides with filter paper on each side (to allow diffusion of fixative) and weighted with a 200 g block (B. McGuire, personal communication). This complex was immersed in 4% paraformaldehyde in 0.1 M phosphate buffer with 30% sucrose for approx. 12 hr. After this time the slice was sufficiently flattened and was cleared in 0.1 M phosphate buffer with 40% sucrose (no paraformaldehyde) for 12–20 hr.

The cortical tissue was then cut on a freezing microtome in 25 μm-thick sections, and each section was placed in a sugarless solution of 0.1 M phosphate buffer.

Cytochrome oxidase reaction

Sections were rinsed 3–4 times in 0.1 M phosphate buffer, and transferred to the reaction medium (100 ml solution of 20 mg catalase, 30 mg cytochrome C, 50 mg diamino benzidine, 100 ml 0.1 M phosphate buffer at 38°C). The container was covered with Saran Wrap to prevent fluid loss. Sections were periodically checked during the course of the reaction, and removed from the reaction medium when the blobs were easily visible. This reaction usually took 18–24 hr to complete. Sections were then rinsed 3–4 times in 0.1 M phosphate buffer solution and mounted on gelatinized glass slides in 0.1 M PB. When sections were dry, cover-slips were placed over them using Permount (Fisher).

Electrode track reconstruction

Electrode tracks were reconstructed with a camera lucida. Each cortical section was traced upon a single acetate sheet, and the location of lesions was carefully noted. When all sections had been traced, the electrode track could be seen by aligning all the acetate sheets using blood vessels as fiducial marks, and observing the stack on a light box. The aligned electrolytic lesions could then be used to reconstruct the path of the electrode track. A track diagram was traced to a single acetate sheet, noting all lesions and cell locations. This diagram was used to label cell locations on video images of each tissue section prior to the densitometry procedures.

We assigned positions of each recording site based upon the location of the lesions in the tissue. There are two possible sources of error in locating cell positions. The first is anisotropic shrinkage or stretching of the cortical tissue during histological processing. This will cause an over- or under-estimate of distances between lesion sites, which subsequently could affect the determination of cell locations. The second source of error is the course the electrode itself takes in its cortical penetration. If tissue dragging prevented the electrode from moving through the cortex in a smooth, continuous fashion, errors could be introduced in the determination of cell positions.

We assessed the magnitude of the error in locating cell positions as follows: for each animal we lined up the lesion locations recorded by micrometer during the experiment with the lesion locations observed in the tissue. This was done by least squares fit of "observed" vs "recorded" lesion locations. The SE was then determined as the root mean square of the residual errors at each lesion location.

Densitometry

We developed a computer program for assessing CO density. Each tissue section was imaged onto a charge-coupled device camera (Hamamatsu Model XC-77) and digitized using an image-capture board (Data Translation DT2855), which allows 8-bit resolution (256 gray-scale). Voltages from the camera were linearized by an input look-up table, which was determined by measuring known luminance values and plotting them as a function of camera output for each known luminance. The effects of uneven illumination were removed by dividing each captured image by a previously obtained image of the blank illumination field. Digital processing of images was performed as follows.

Artifact removal. To minimize the contamination of the density measurements by large vessels and other
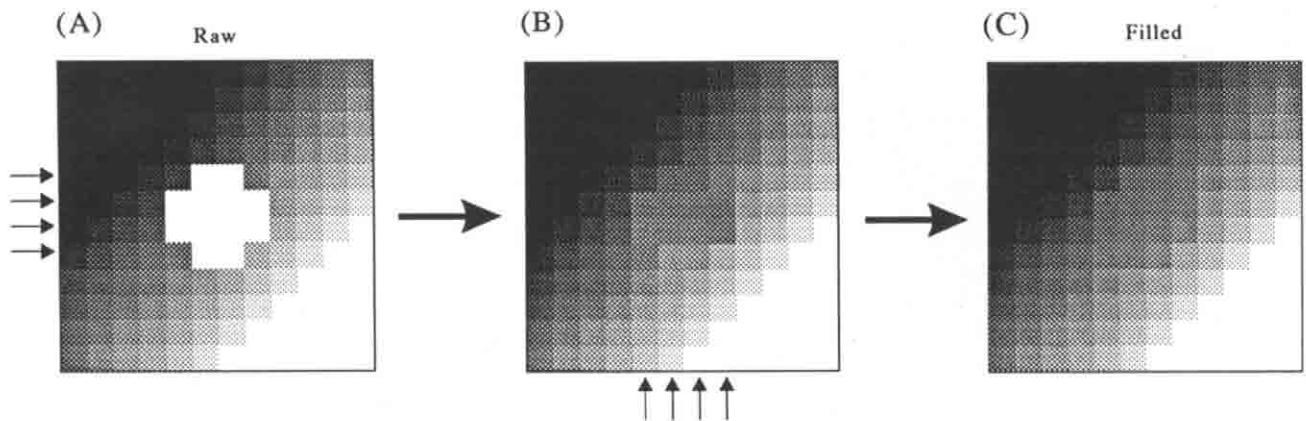
FIGURE 2. Illustration of the artifact removal procedure. (A) Each horizontal line in the artifact is filled with the mean of 4 pixels on each side of the artifact. If a pixel in the calculating region is also outside the density limits, a pixel further out is used in the calculation. (B) A similar procedure is applied to each vertical line of the artifact, except that each pixel in the artifact is now assigned the average of the vertical and horizontal means. (C) Final result. Small arrows indicate lines to be filled.

debris, the computer performed a search for areas with extreme density levels which were either darker than the darkest blobs or lighter than the lightest interblob regions. These areas were filled with the average density of surrounding tissue as shown in Fig. 2.

Image flattening. To allow a more accurate measure of relative CO density, a mask (650 μm square) was passed over the image. At each position, the average density within the mask was computed, and subtracted from a 32 μm square block in the center. The mask was then moved 32 μm, and the procedure repeated until the mask had moved over the entire image. The result was the original image with slowly-varying gradients (with periods > 1300 μm) removed.

Contrast enhancement. A simple histogram expansion was performed on the image to improve its visibility. This was necessary since the density values after artifact removal were typically spread over a gray-scale range of 80–140, while the possible gray-scale values are from 0 to 255. The image densities were therefore normalized to fit this full 0–255 range.

Smoothing. To remove artifacts due to capillaries and small debris, the images were smoothed with a triangular filter mask with a half-height of 65 μm.

Assignment of density and distance information to recording sites

For each electrode recording position, the nearest blob was found by a computer search of the density terrain. The search algorithm was a modified version of the Simplex fitting algorithm (Caceci & Cacheris, 1984). The center pixel of the nearest blob was computed as the centroid of the density colour found by the Simplex algorithm. Two quantities were then determined for each recording position. (1) Distance to nearest blob center. This was a straightforward geometrical calculation, since the (x, y) locations of the recording site and the nearest blob center were known. (2) Density relative to the nearest blob center, $\rho = (\rho_r - \rho_{ib})/(\rho_b - \rho_{ib})$, where ρ_r is the optical density at the recording site, ρ_b is the optical

density of the nearest blob peak, and ρ_{ib} is the interblob density, determined as the median of nine low-density regions surrounding the nearest blob. Distance and relative density were then used for correlations with the physiological measurements of spatial frequency response and contrast sensitivity.

An image processing example: assessment of blob density profiles

For three monkeys, blob density profiles were examined to determine the nature of the transition between blob and interblob zones. We show here the steps taken in assessing these profiles for one of the three monkeys. Figure 3(A) shows the raw image taken from a tangential section of macaque visual cortex. Several factors must be considered before an accurate assessment of CO density can be obtained. Here we show three types of contamination artifacts. (1) Large vessels, which run orthogonal to the plane of section, appear as white dots. (2) The network of small pale streaks seen in the figure are capillaries which run horizontally through the plane of section. Since capillaries displace neural tissue, the presence of a capillary is marked by a lightly-staining streak. These capillaries often do not span the whole depth of the section, and can be over- or underlaid by neural tissue. (3) High density artifacts (usually indicating stray lymphocytes) appear as small black dots.

The large blood vessel artifacts can usually be removed, since they are much less dense than the range of interest. Figure 3(B) shows the raw image after it has been passed through the artifact removal routine.

Even after digital removal of the large vessel artifacts, it can be seen that the image is noisy. It is difficult to determine the true density variations in the neuropil of the blobs, because the neuropil thickness varies across the section as a result of interruption by the small capillaries. The traditional way of removing high-frequency variations is to pass a smoothing mask over the image, which results in a low-pass filtered version of the image. However, sharp edges are rounded off by this
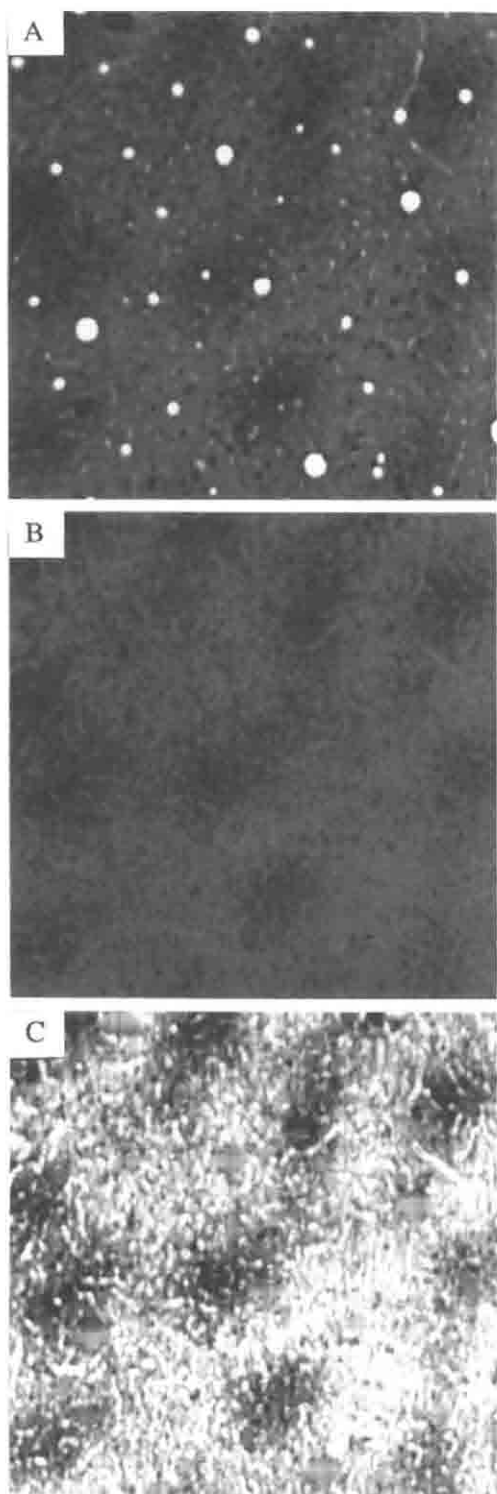
FIGURE 3. Analysis of raw images of monkey cortex. (A) 25 μm tangential section of opercular cortex. Cortex was flattened prior to cutting to ensure perfectly tangential sections. Large blood vessels appear as white dots; a network of smaller, horizontally running capillaries can be seen running throughout the section. (B) Artifact removal. Areas which lie outside of user-determined limits are filled in with the average of surrounding density values. (C) Contrast enhancement.

technique. If blobs have sharp edges, such smoothing will distort their shape, and we wished to avoid such distortions.

Contour smoothing. A novel approach was developed to remove density artifacts caused by capillaries and scattered blood cells without changing the radial fall-off in density from blob centers. Contour smoothing was accomplished via the following steps (see Fig. 4):

(1) The contrast enhanced image (here called the raw image) was convolved with a two-dimensional mask, resulting in a low-passed image. The mask had a weight of 100% in the center, which decreased linearly to 0% at a distance of 47 μm from center. The convolution was obtained by moving the mask over the image 1 pixel at a time. At each position, the weighted sum of all pixels within the mask was computed and assigned to the center pixel.

(2) A contour map of the low-passed image was then constructed. Consider a contour line circling a blob at a density level ρ: this contour line describes the intersection of a horizontal plane at density ρ passing through the blob. Contour smoothing assumes that this cross-sectional shape accurately depicts the shape of the actual blob.

(3) Each contour line (calculated from the *low-pass* filtered image) was then used as a template for smoothing the *raw* image. First, the contour was placed in its corresponding position on the raw image. The values of all pixels covered by the contour template were then collected. From these values a median value was calculated. The contour was then placed in its corresponding position on the final image, and the median density value was assigned to each pixel covered by the contour. This procedure was repeated for each contour until every pixel in the final image was assigned.

Contour smoothing utilizes the horizontal cross-sectional blob shape determined from the smoothed image. The pedestal simulation in Fig. 4 indicates that this shape is preserved remarkably well [cf. the shape of pedestal functions in Fig. 4(D) with their corresponding shapes in the noisy panel, Fig. 4(C)]. It is important to emphasize that our contour smoothing preserves the sharpness of the density gradient. This is possible because the smoothing is done tangentially with respect to the blob, rather than radially.

RESULTS

Cytochrome oxidase density distribution

Figure 4 shows the results of contour smoothing on real cortical data and on a simulation using pedestal functions, in which CO density changes abruptly. The vessel contamination of the pedestal image is removed in the result, with very little effect upon the sharpness of the pedestal borders. Note also that the shapes of the pedestals undergo minimal distortion in the procedure. Application of contour smoothing to the raw data therefore gives an accurate representation of the blob density profiles. It is clear from Fig. 4(B) that the density profiles fall off gradually with distance from blob centers.

Cortical tissue

Pedestal simulation
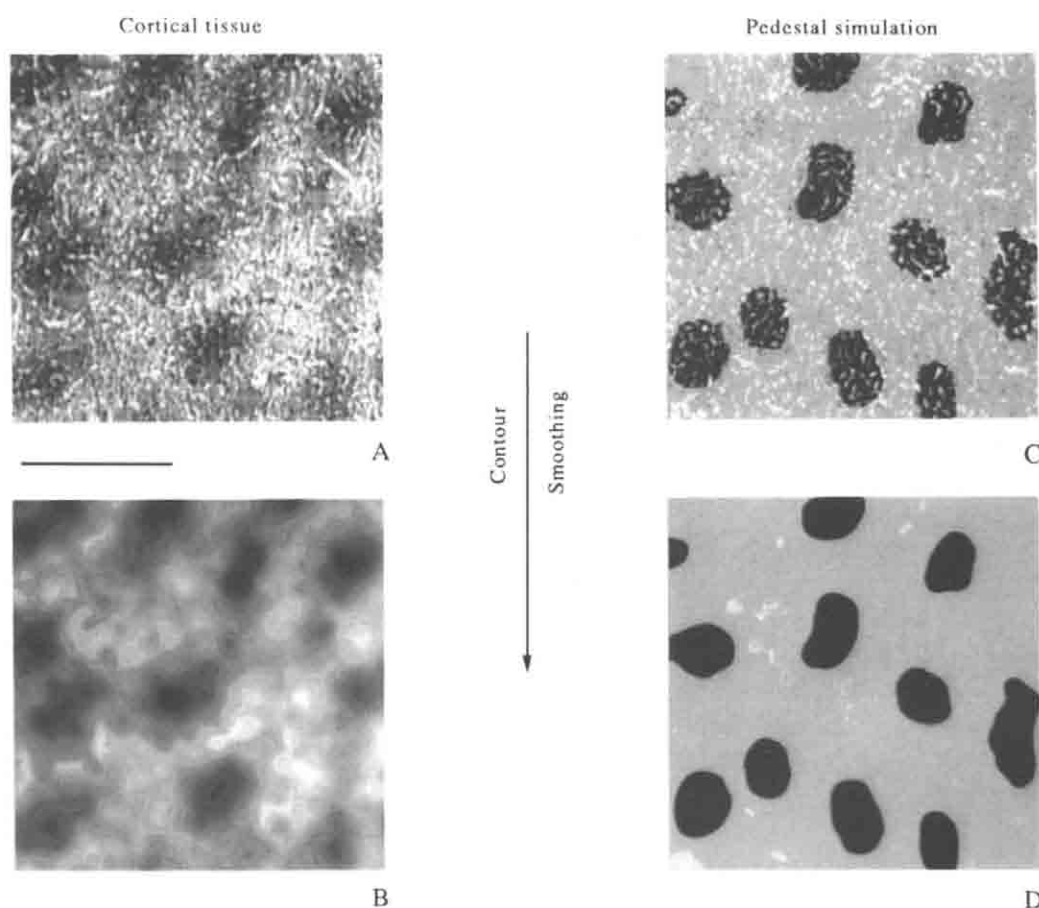

A

C

B

D

Contour

Smoothing

FIGURE 4. Contour smoothing. (A, B) The results of contour smoothing on the raw image. Contour smoothing was done by determining contours for each blob using a low-pass filtered version of the raw image, then calculating the median density for each contour from the raw image and assigning the median density to each contour pixel in the result. (C, D) The effect of this procedure on pedestal-like functions which are contaminated by capillary-like artifacts. Note that while the artifacts have been successfully removed, there is very little blunting of the pedestal edges, a result not obtainable by traditional low-pass smoothing methods or median filtering.

The accuracy of the contour smoothing routine decreases near blob peaks, since the number of pixels per contour is greatly reduced, and local variations in optical density are more likely to affect the determination of median density.

Color map. Figure 5 is a three-dimensional representation of a section of Fig. 4(B). It is shown in pseudo-color to indicate the various density levels across the image. There are several points to note about this image. (1) Blobs can be seen in several forms: in isolation, connected by bridges (Horton, 1984; Ts'o & Gilbert, 1988), or nearly confluent with one another. (2) The peak density varies somewhat from blob to blob. (3) The interblob regions, far from being of uniform density, more closely resemble canyons dipping into low-density regions. (4) Many blobs have an elliptical shape. (5) Some blobs appear to have steep sides, but, in general, their density decreases gradually with distance from the centers.

Individual cross-sections. Figure 6 shows several examples of the density profiles across individual blobs. It can be seen that the form of the profiles differs considerably from blob to blob. Some drop off more rapidly than others. Some resemble triangular functions,

whereas others are better approximated by a Gaussian profile.

Slopes. In order to quantify the steepness of the CO density fall-off, we examined cross-sections from 64 blobs from three monkeys. Cross-sections were taken from the contour-smoothed images in each case. Each blob was represented by 18 cross-sections, taken radially at 20-deg intervals. Blob center was determined by the location of peak blob density, and interblob position was determined as the location of lowest density. For the density profile along each radius we then calculated the range of densities from 25% to 75% of the total blob-to-interblob extent. Points in this range were fit with a straight line, and the slope of this line was our steepness measure. The histogram of slopes from all monkeys is shown in Fig. 7. The distribution of slopes is very similar for the three monkeys, as are the median slopes (monkey 1, $0.51\%/\mu$m; monkey 2, $0.60\%/\mu$m; monkey 3, $0.52\%/\mu$m). The data in Figs 2–4 are from the monkey with the steepest slope (No. 2).

Figure 8 shows the range of slopes that were typically seen in our sample. The hatched area indicates the range of slopes between lower and upper quartile range for blobs from all three monkeys. This shows that the CO
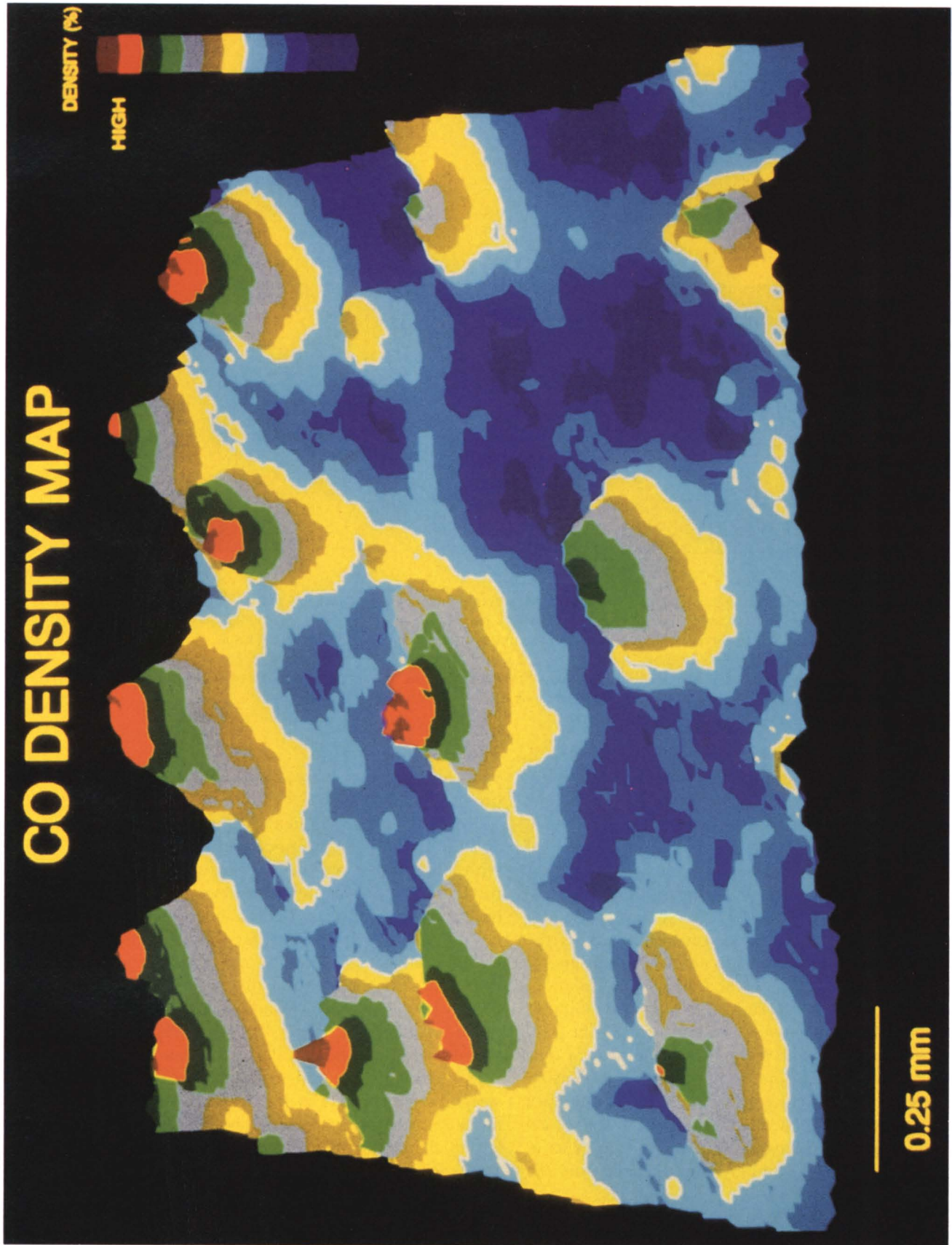
FIGURE 5. Pseudocolor representation of density map. This image is taken from a section of the image of Fig. 4. The color bar shows the color progression from low to high density. Varied density profiles of blobs are evident. Note that the uppermost blob profile is essentially triangular, whereas the blob in the lower left drops off very quickly on the right side.
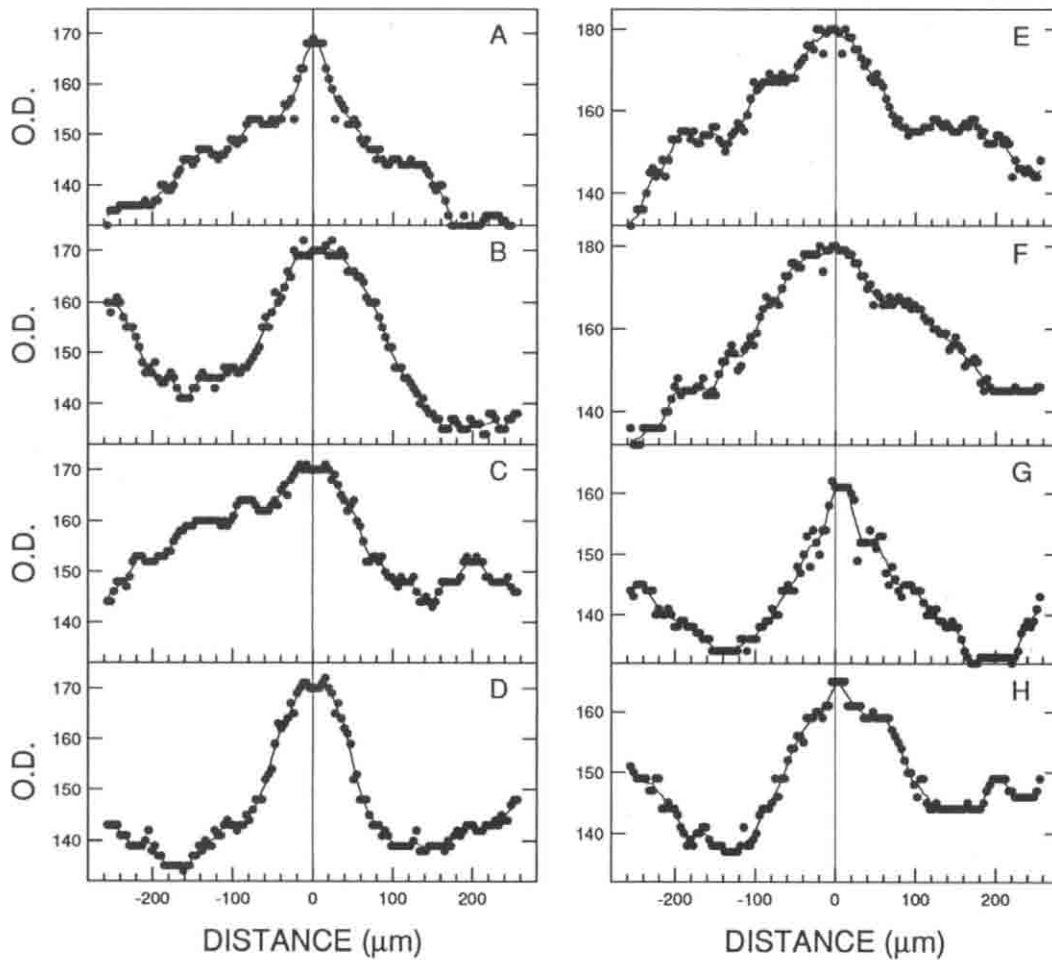
FIGURE 6. Eight examples of blob density profiles. Data were obtained from cross-sections of blobs in contour-smoothed images. Width at half-height ranges from approx. 100 μm (D) to 200 μm (C, F). Blob peaks can be sharp (A, G), or rounded (B, F). The nature of the density fall-off varies from linear (G) to Gaussian-like (D) to mixed (C). With all their varied features, all blobs have in common a gradual decrease in density from centers outward.
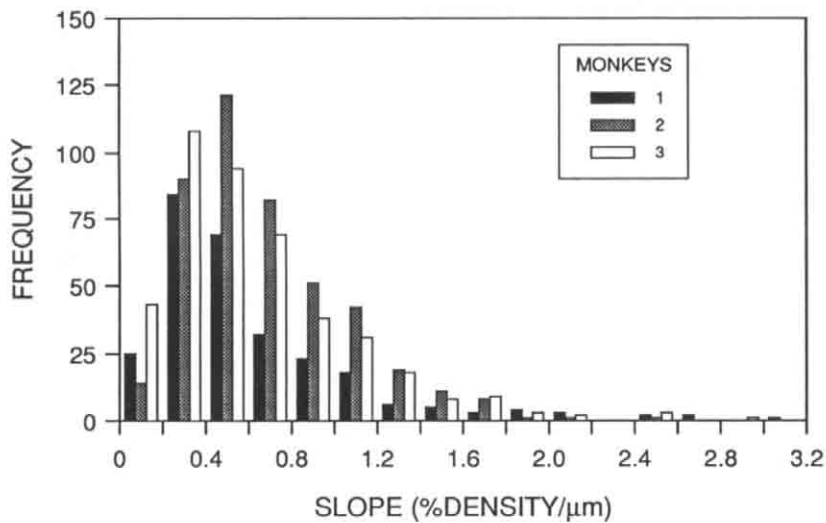

FIGURE 7. Histogram of blob slopes. Slopes are for 18 radial sections through each blob of three monkeys. For each radial section the slope was determined by the least-squares linear fit through points having densities between 25% and 75% of peak blob density. Median slopes are 0.51 for monkey 1, 0.60 for monkey 2, 0.52 for monkey 3, and the median slope for all blobs in combination is 0.55.
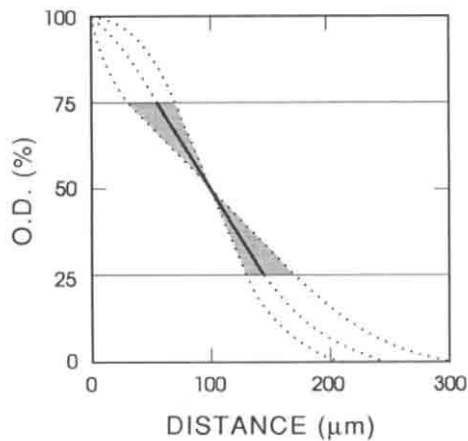
FIGURE 8. Illustration of range of slopes seen in blobs. Steepest slope is the upper quartile (0.86%/μm), bold line is the median slope (0.55%/μm), least steep slope is the lower quartile (0.36%/μm). Dotted lines show typical blob shapes through each of these three slopes. Width at half-height was arbitrarily fixed at 100 μm for ease of comparison.

density in blobs typically decreases *gradually* from blob center outward, a finding that agrees with those of Trusk, Kaboord and Wong-Riley (1990).

Contrast sensitivity

The ability of a neuron to detect a stimulus reliably depends not only on its response magnitude, but also on the *variability* of the response, a response aspect which is not accounted for by the contrast gain. Contrast sensitivity is defined as the reciprocal of the contrast threshold, the lowest contrast required to detect a stimulus reliably. Contrast sensitivity is a more informative measure of cells' ability to signal contrast than are contrast gain, contrast threshold or response amplitude. This is because contrast sensitivity makes use of the response variance, and allows a comparison of single unit data with psychophysics. Therefore here we use contrast sensitivity as a measure of cell performance.

We recorded responses to patterns of various contrasts from neurons in nine tracks in seven monkeys. The histological reconstructions from three of these monkeys were not clear enough for a confident assignment of CO density to the recording sites, so 58 cells from six tracks in four monkeys were actually used for analysis.

Lateral geniculate. Figure 9 shows contrast sensitivity data for three typical parvocellular neurons. The response vs contrast functions have logarithmic abscissas in order to compare them directly with the logarithmic form of the neurometric function. As shown by Purpura, Kaplan and Shapley (1989), the response variance is independent of contrast. Note that while the response vs contrast functions for all three neurons are similar in shape, the neurometric functions are right-shifted in proportion to response variance. Therefore, evaluating cells' performance using only response magnitude (Hubel & Livingstone, 1990) produces a different result from that given by the neurometric functions.

Figure 10 compares contrast sensitivity data for a magnocellular neuron and a parvocellular neuron.

Again, note the constant response variance across all contrasts. The contrast sensitivity of the magnocellular neuron (*A*) is 0.20 and that of the parvocellular neuron is one-tenth of that (0.02). An interesting feature of the magnocellular neurometric function is that it begins to saturate past 20% contrast, while the response amplitude continues to increase with contrast. This is because the signal and signal + noise PNDs are almost completely non-overlapping at contrasts higher than 20%. Recalling that non-overlapping PNDs result in a detection probability of 1.0, we see that further separation of the PNDs will increase the response, but not the detection probability.

Cortical layers 2/3. Figure 11 shows response vs contrast functions for several cortical neurons. Note that the response variance of these cortical neurons increases with stimulus contrast (Tolhurst *et al.*, 1983), unlike the behavior of retinal ganglion cells (Croner *et al.*, 1993) or of geniculate neurons (Purpura *et al.*, 1989). The shapes of neurometric functions in Fig. 11 vary widely in comparison to the corresponding response vs contrast functions. This is due to the response variance, which has a profound effect on the detection probability. The neurometric functions for seven cells never reached 75%, even at the maximum contrast. The contrast sensitivity for these cells could not, therefore, be determined.

Many cortical neurons have little or no spontaneous discharge. One might surmise that such neurons would be perfect detectors if they fire even weakly in response to a stimulus. This is rarely the case, however. Even if this type of neuron responds quite strongly to the stimulus, it may not fire during *every* trial, in which case the signal and signal + noise distributions still overlap, resulting in less-than-perfect detection.

Cortical vs geniculate contrast sensitivity. In order to compare the contrast sensitivities of cortical and geniculate neurons, we subjected seven magnocellular neurons and 16 parvocellular neurons to the identical ROC analysis we used for cortical neurons. Table 1 compares the means and SDs of contrast sensitivities for geniculate neurons and those from layers 2/3. On average the contrast sensitivity of neurons in layer 2/3 resembles that of parvocellular neurons, although there are a few cortical neurons with fairly high contrast sensitivity, similar to that of magnocellular neurons.

Contrast sensitivity and CO blobs. Figure 12 shows the contrast sensitivity of each neuron as a function of distance from blob centers. The data on both contrast sensitivity and spatial frequency were more tightly correlated with distance than with relative CO density, so we present these data as a function of distance. Contrast sensitivities of neurons near blob centers (0 μm) are spread over a broad range of contrasts: cells with both high and low sensitivities are found near blob centers. However, as one moves away from blob centers, the range of sensitivities decreases, until, in the interblob regions, only cells with low sensitivity are found. Recall that the contrast sensitivity is measured from the fitted neurometric function, and is determined by the lowest contrast that could produce a 75% detection probability.

CONTRAST RESPONSE
(& RESPONSE VARIANCE)
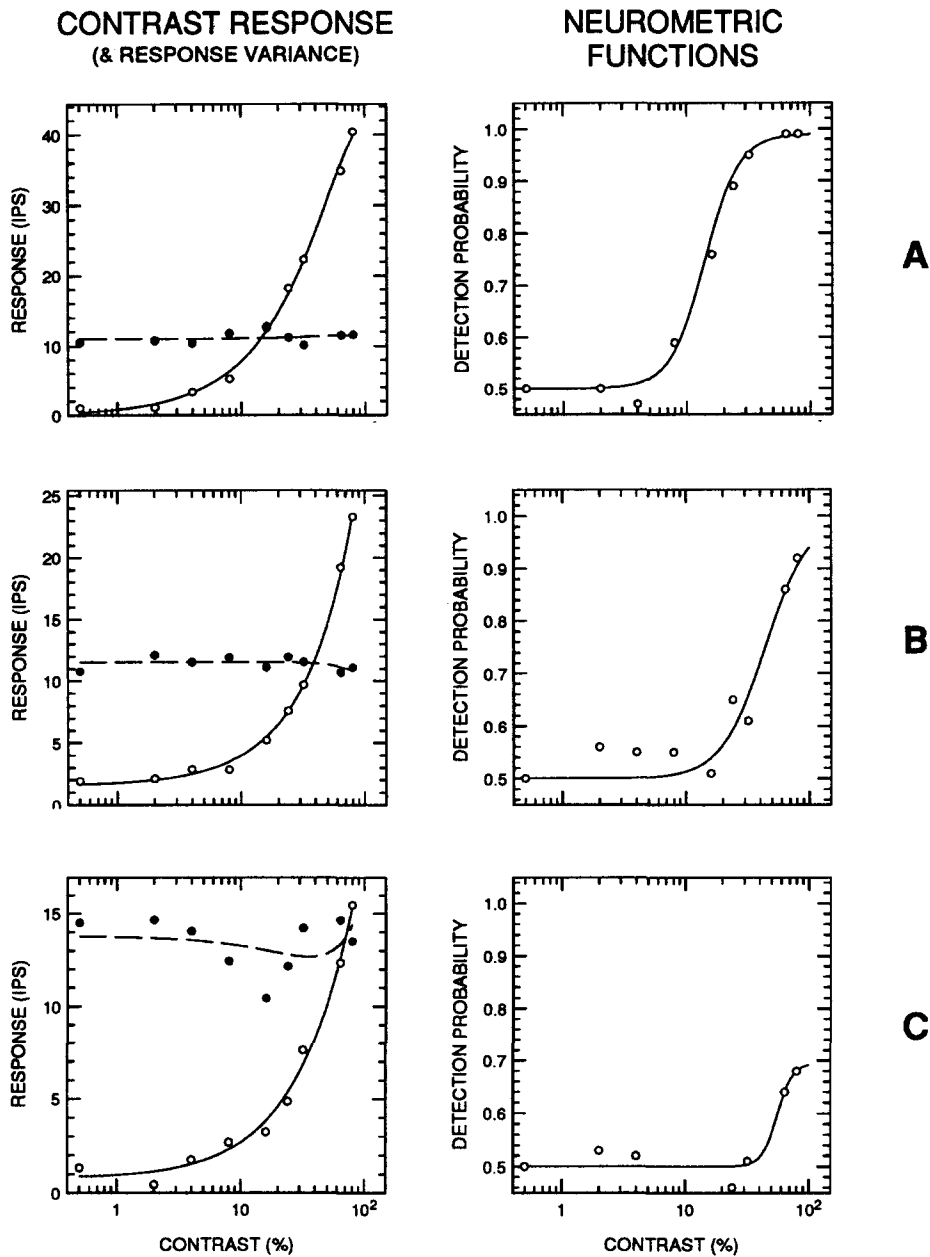
NEUROMETRIC
FUNCTIONS

FIGURE 9. Response vs contrast functions and associated neurometric functions for three parvocellular neurons. Left panels: open symbols indicate response in impulses per second (ips), solid symbols indicate response variance (in ips^2). Right panels: neurometric functions, calculated as described in Fig. 1. Note that the response vs contrast functions for (A)–(C) are similar, while the neurometric functions are very different. Neurometric functions are shifted on the abscissa according to the response variance.

The mean contrast sensitivities of magnocellular and parvocellular geniculate neurons are indicated by dotted lines in Fig. 12. Neurons with parvo-like contrast sensitivities are spread fairly evenly throughout, while those with magno-like sensitivities are found only near blob centers. In addition, rather than dropping abruptly at blob "borders", the contrast sensitivity of these magno-like cells also decreases *gradually* with distance from blob centers.

Ensemble performance. Several cells in our sample (7 out of 58) did not reach a detection probability of 75%, even at the maximum contrast. Therefore the conventional measure of contrast sensitivity is not sufficient to account for these data. An examination of the neuromet-

ric functions of these cells shows that, although they did not reach 75% probability, they did respond at greater than chance levels. To account for these cells, we plot maximal detection probability for each cell as a function of distance from blob center for several contrasts (Fig. 13). The size of each dot represents the detection probability for an individual cell, plotted according to distance from blob center, at a randomly assigned angular position. All the cells are displayed *as if* they all came from the same blob/interblob region. The dashed circle has a diameter of 200 μm.

Obviously, pooling the data in this manner ignores differences among blobs and among animals, but the picture that emerges is useful. At low contrasts (1–4%),
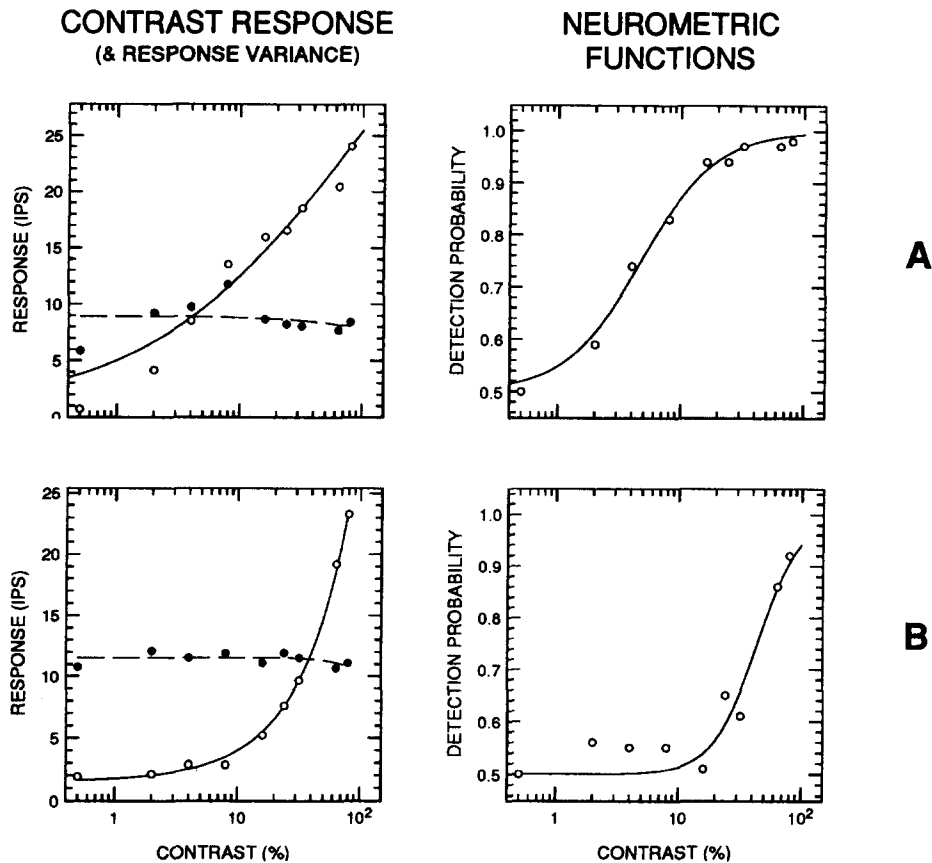
FIGURE 10. Response vs contrast functions and associated neurometric functions for a magnocellular (A) and parvocellular (B) neuron. Left panels: open symbols indicate response (ips), solid symbols indicate response variance (in ips^2). Right panels: neurometric functions, calculated as described in Fig. 1. Note that the neurometric function of the magnocellular neuron begins to rise at low contrasts compared to the neurometric function of the parvocellular neuron.

detection of patterns is very poor in both blob and interblob regions. Starting at 8% contrast, however, some cells near blob centers begin to detect the pattern (indicated by the larger dots). As contrast increases, some interblob cells begin to detect the stimulus until, at 96% contrast, all cells reach their maximal detection probability.

Again, it can be seen that the cells with the highest contrast sensitivities are those near blob centers. At contrasts from 8% to 16% the blob centers dominate, and only at higher contrasts do the interblob cells begin to detect the stimulus. This illustration of the ensemble performance underscores the important point that not *all* cells in the blobs are highly sensitive. In fact, the majority (75%) of these cells are quite poor at detecting low-contrast stimuli, despite our careful optimization of the stimulus parameters.

Spatial frequency

If a subpopulation of cortical cells is devoted to spatial analysis, it is of interest to characterize the spatial properties of the receptive fields of these neurons. We therefore measured spatial tuning curves for 74 single cells and 45 multi-unit recordings from five animals. Figure 14 shows representative spatial tuning curves taken from single units near blob centers ($<100\,\mu$m) and in interblob regions ($>200\,\mu$m). The majority of

these cells exhibit band-pass tuning characteristics (De Valois *et al.*, 1982a), with varying bandwidths. Note that the optimal spatial frequency of blob cells falls within a fairly narrow range, while the optimal spatial frequency of cells in the interblobs shows much greater variability.

Optimal spatial frequency. In Fig. 15 we plot optimal spatial frequency as a function of distance from blob center. Single-unit and multi-unit data are first plotted separately, and then combined in Fig. 15(C). Except for a few scattered points in the single-unit data, both single- and multi-unit data are very close in their distributions, so we concentrate on the composite plot in Fig. 15(C). Figure 15(D) is a box-and-whisker plot for the combined single and multi-unit data in Fig. 15(C). It shows a clear increase in the *range* of optimal spatial frequencies as one moves away from the center of the blobs. The height of each bar denotes the interquartile range (IQR) for each 100 μm bin. The interquartile range contains the middle 50% of the data. Cells in the bin nearest blob centers are confined to a narrow range of optimal spatial frequencies (IQR = 1.5 c/deg from 0–100 μm; IQR = 3.3 c/deg from 200–300 μm). These data are consistent with previous studies in that cells near blob centers are tuned to low spatial frequencies and the mean optimal spatial frequency increases with distance from blob center. Our data, like those of Born and Tootell

CONTRAST RESPONSE
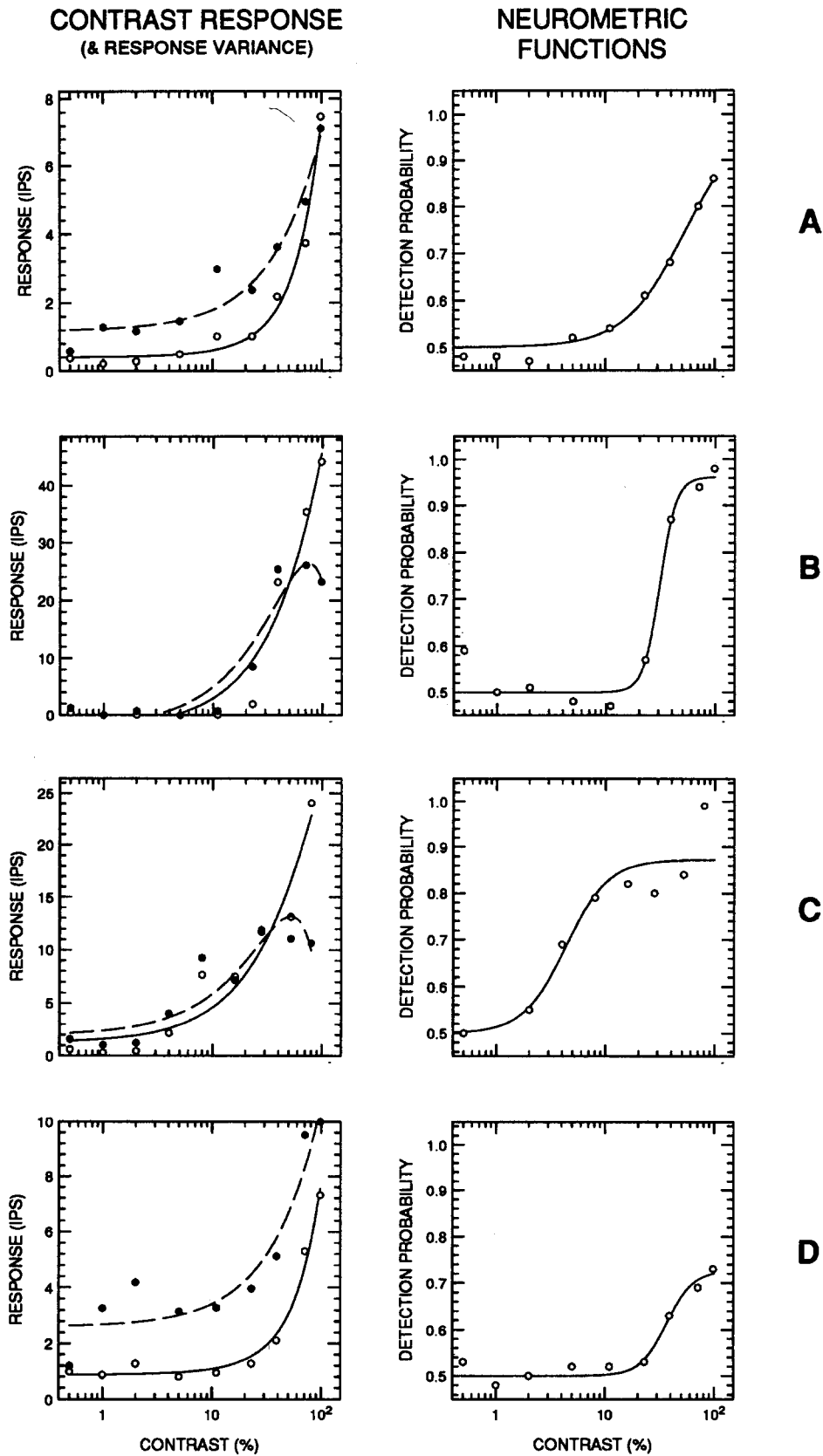## (& RESPONSE VARIANCE)

NEUROMETRIC
FUNCTIONS

FIGURE 11. Response vs contrast functions and associated neurometric functions for several cortical neurons. Left panels: open symbols indicate response (in ips), solid symbols indicate response variance (in ips^2). Right panels: neurometric functions, calculated as described in Fig. 1. Note that responses for all cells continue to increase up to the highest contrast, without any sign of saturation. The neurometric functions vary in shape. (C) The most sensitive cell of the four, reaching the criterion detection probability (0.75) at 6% contrast. (D) Clearly responsive, but never reaches the criterion.

TABLE 1. Comparison of contrast sensitivities of geniculate neurons and neurons in layers 2/3 of striate cortex

	Mean	SD	*n*
Layers 2/3	0.034	0.030	51
Parvo	0.035	0.040	16
Magno	0.158	0.079	7

Mean contrast sensitivities for layers 2/3 neurons and parvocellular neurons are very similar. Magnocellular neurons' contrast sensitivities are much higher. Contrast sensitivity is defined here as the reciprocal of the contrast that produced 75% probability of detection.

(1991a), show a significant proportion of interblob cells which are tuned to low spatial frequencies.

Note the nature of the tuning far from blob center [Fig. 15(C)]. Although only a few cells were found past 300 μm, five out of seven of these cells were tuned to high spatial frequencies. This suggests that cells tuned to low spatial frequency are relatively rare in regions distant from blob centers.

Note again, that the change in optimal spatial frequency is *gradual* as one moves away from the blobs. This could be a physiological correlate for the gradual decline in CO density profiles shown in Figs 4–6. This finding supports the conclusions of Silverman *et al.* (1989), who also found no evidence for an abrupt change in spatial frequency tuning between blobs and interblob regions.

Ensemble response. Figure 16 shows the results of an ensemble response simulation, similar to that shown for contrast in Fig. 13. We utilized the spatial tuning curves

for each cell (response vs spatial frequency), and plotted normalized responses across all distances for increasing spatial frequency. Since maximum response varies widely among recordings (especially in multi-unit recordings), we normalized the spatial tuning curves for each recording such that the response varied from 0 (small dots) to 1 (large dots). Note that some of the dots disappear at higher spatial frequencies. This is because the spatial tuning curves for a small minority of these cells were not recorded at sufficiently high spatial frequencies.
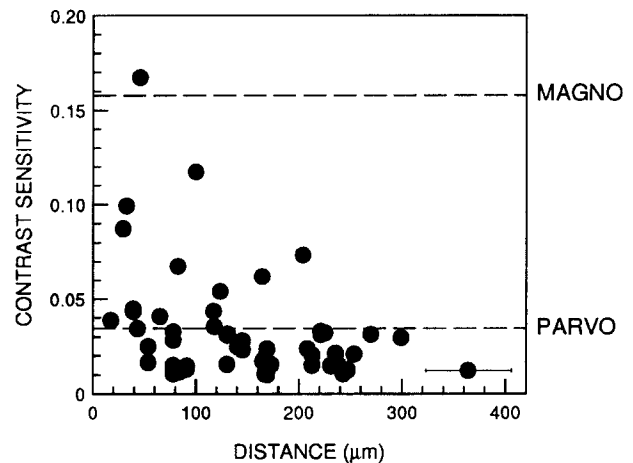

FIGURE 12. Contrast sensitivities of single neurons plotted vs distance from blob centers. The horizontal dashed lines indicate medians of magnocellular and parvocellular contrast sensitivities taken from the neurometric functions of geniculate data. Data shown only for the 51 cortical cells that reached the criterion of 75% detection probability. Error bar indicates the uncertainty in localizing cell position, determined as the SE between recorded and actual lesion positions (see Methods).
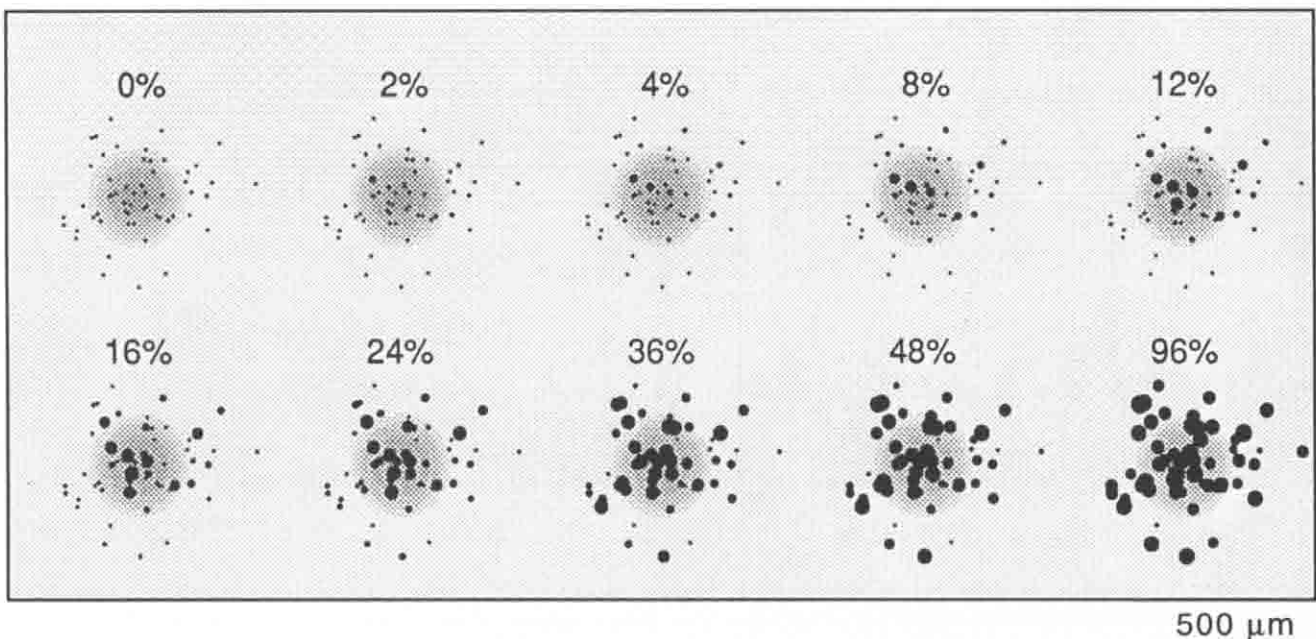

FIGURE 13. Ensemble performance plots for pattern detection. Each cluster represents detection probabilities for a particular value of contrast. In this polar representation, the amplitude signifies the distance of each cell from its nearest blob center and the phase is randomized to provide a view of the "idealized" blob performance. Dot size indicates the detection probability, with the largest dots indicating a detection probability of 1.

BLOB
(<100μ)

INTERBLOB
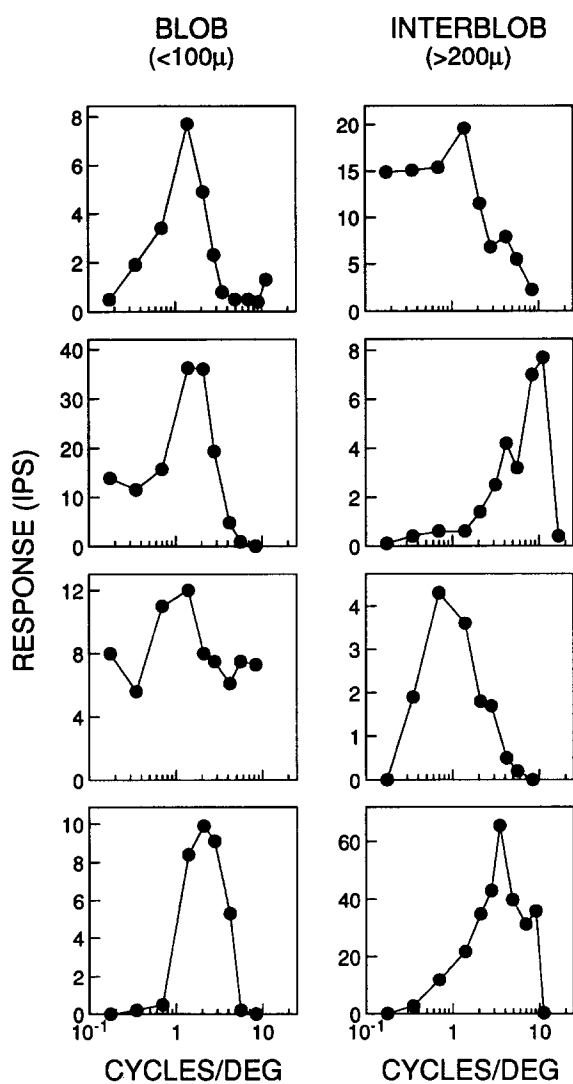(>200μ)

RESPONSE (IPS)

CYCLES/DEG

CYCLES/DEG

FIGURE 14. Examples of spatial tuning curves for four "blob" and four "interblob" single units. Note that the optimal spatial frequency of the blob cells differs less than that of the interblob cells. We have extracted three parameters from the spatial tuning curves: optimal spatial frequency (the spatial frequency at peak response), the cut-off spatial frequency (the spatial frequency at half the maximal response), and bandwidth (the width of the spatial tuning function at half the maximal response).

An examination of the ensemble response simulation shows only a few cells responding at the lowest spatial frequencies. This is because cortical cells are band-pass spatial filters. The first strong ensemble response is elicited at 1.4 c/deg, and active units can be seen near the blob center and farther out. As spatial frequency is increased, the activity of cells near the blob centers slowly drops out, and the ensemble response is dominated by the interblob regions.

There is one aspect of the ensemble response that we might not have predicted from the optimal spatial frequency data: blob centers do not stop responding completely until the spatial frequency is quite high. This is because the optimal spatial frequency does not provide a complete measure of the performance for these cells. The performance of a filter is typically characterized by several parameters: the optimal response, the cut-off frequency, and the bandwidth at half-maximal response.

Cut-off spatial frequency. An examination of the cut-off spatial frequency for each recording (Fig. 17) helps to explain the neural ensemble response as spatial frequency increases (Fig. 16). The cut-off spatial frequency determined from contrast sensitivity functions gives the resolution limit of a cell. Due to time constraints, we determined cut-off spatial frequency from spatial tuning curves, and can therefore only consider our measure to be an approximation of the resolution limit. While the optimal spatial frequency increases quite gradually into the interblob regions, the cut-off depends more strongly on distance from the blob center, and some cells near the blobs respond at fairly high spatial frequencies. Note that there is a significant correlation of cut-off spatial frequency with distance-to-center ($r_s = 0.19$, $n = 110$, $P < 0.002$).

There is a substantial difference between cut-off frequencies of single cells [Fig. 17(A)] and cut-off frequencies of multi-unit recordings [Fig. 17(B)]. Only a few single units respond above 8 c/deg, whereas more than half of the multi-unit recordings do so. This may be due to a sampling bias of the electrodes: in order to unequivocally isolate single units, it was necessary to accept only

(A) Single units   (B) Multi-unit activity   (C) All   (D) All
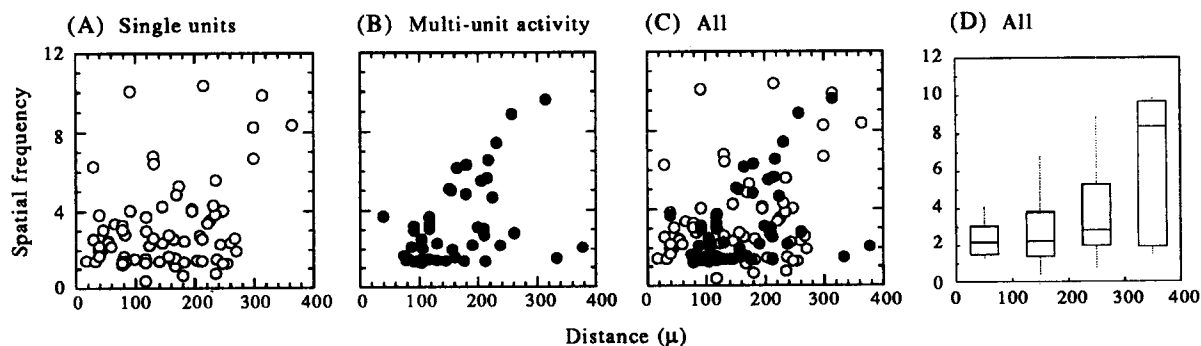

Spatial frequency

Distance (μ)

FIGURE 15. Optimal spatial frequency plotted vs distance to blob centers. (A) Optimal spatial frequencies of isolated units are plotted vs distance-to-center. (B) Multi-unit recordings (three or more units). (C) Single- and multi-unit recordings combined. (D) Box-and-whisker plot representing binned data from (C), Each vertical box represents the interquartile range, or the middle 50% of the data values from each 100 μm bin. The "whiskers" extend to 1.5 times the interquartile range. The central horizontal line is the median value. Medians for each bin: 2.2, 2.4, 2.9, 8.3 c/deg.
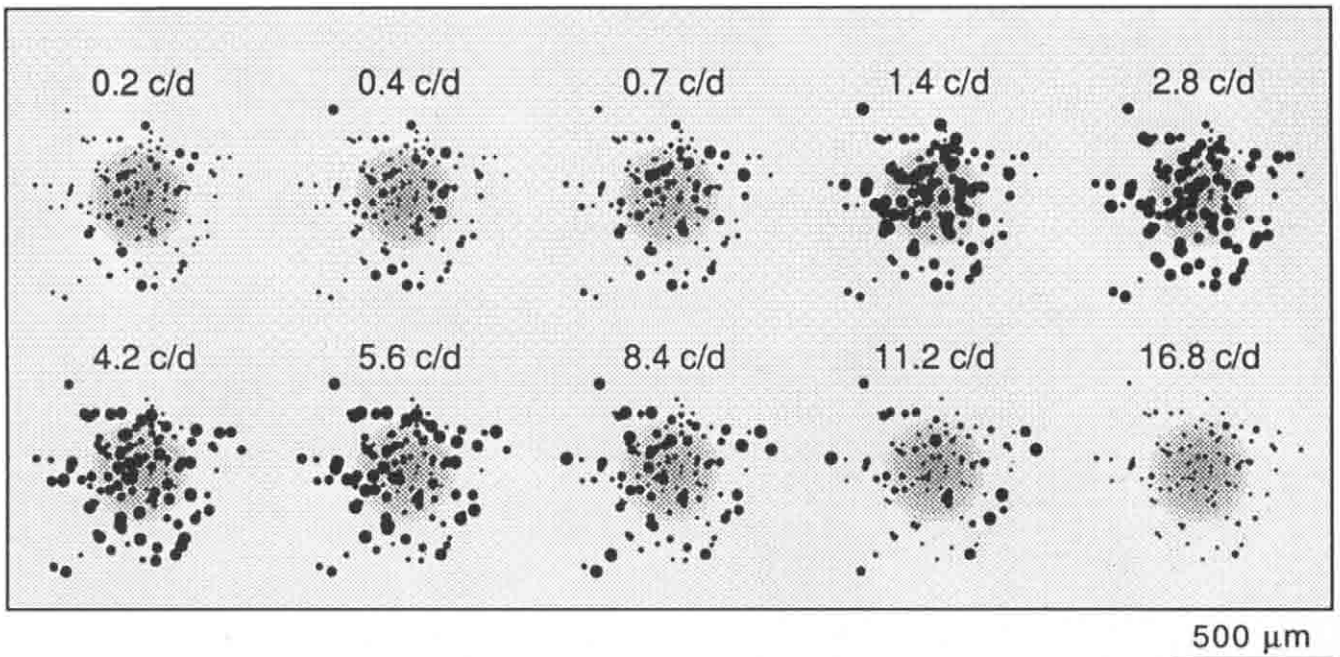
FIGURE 16. Ensemble response to several spatial frequencies. Each cluster represents normalized response at a particular spatial frequency. In this polar representation, the amplitude signifies the distance of each cell from its nearest blob center and the phase is randomized to provide a view of the "idealized" blob performance. Spatial tuning curves for each recording were normalized so that response varied from 0 (small dots) to 1 (large dots).

units with spike amplitudes well above the multi-unit activity. It is conceivable that those neurons which are tuned to lower spatial frequencies are larger, and thus more easily isolated. However, a multi-unit recording accepts units with smaller spikes, and it appears that these often correspond to higher cut-off frequencies. In addition, the cut-off frequency for multi-unit recordings reflects the cut-off frequency of the unit with the best spatial resolution—information is lost about cells in the multi-unit response which cut off at lower spatial frequencies. The box-and-whisker plot in Fig. 18 shows a fairly clean separation of cut-off frequencies between cells near the blobs (bin 0–100 μm) and cells farther away (bin 200–300 μm; however, the right-most bin contains only three cells).

Bandwidth. The spatial frequency bandwidth was the only parameter of the spatial transfer function which showed no significant correlation with distance to blob center.

DISCUSSION

Blob density profiles

Most blobs do not have distinct borders, and show a gradual fall-off in density from the center outward. This then raises the question: how does one determine the extent of the blobs? This is especially important in studies in which cells are classified as belonging to "blobs" or "interblobs". One reasonable measure often
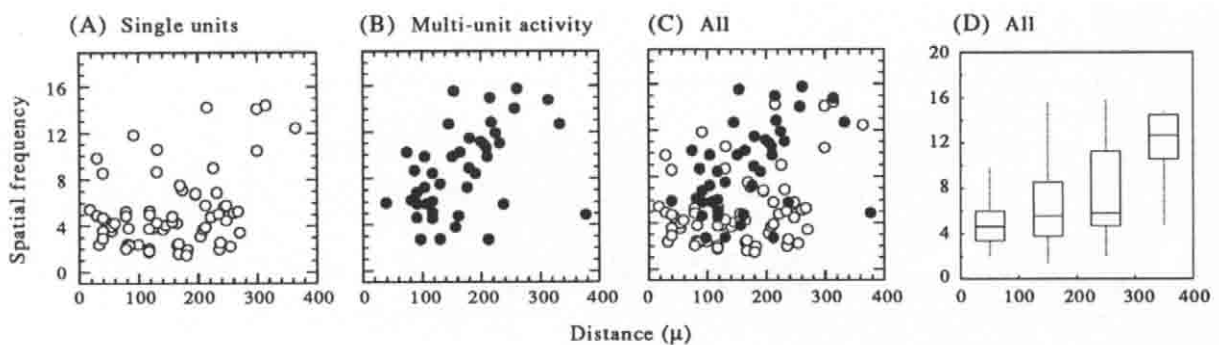

FIGURE 17. Cut-off spatial frequency plotted vs distance to blob centers. (A) Cut-off spatial frequencies of isolated units are plotted vs distance-to-center. (B) Multi-unit recordings (three or more units). (C) Single and multi-unit recordings combined. (D) Box-and-whisker plot representing binned data from (C). Each vertical box represents the interquartile range, or the middle 50% of the data values from each 100 μm bin. The "whiskers" extend to 1.5 times the interquartile range. The central horizontal line is the median value.
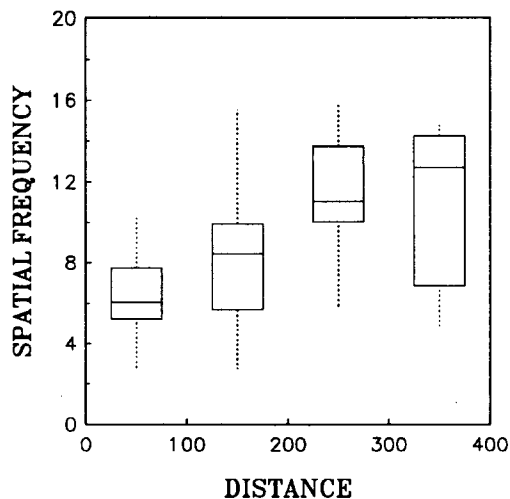
FIGURE 18. Cut-off spatial frequency vs distance from blob center. Box-and-whisker plot representing binned data from Fig. 17(B) (multi-unit activity). Each vertical box represents the interquartile range, or the middle 50% of the data values from each 100 μm bin. The "whiskers" extend to 1.5 times the interquartile range. The central horizontal line is the median value.

used in other applications is that of width at half-maximal amplitude. A quantitative measure of this sort would be useful in the determination of blob areas, or of blob shapes, and can readily be obtained using the methods described here. A subjective drawing of blob "borders" would certainly require less effort, and could be used in applications which do not require a high degree of accuracy in the density measurement.

It is not surprising that blobs have gradually decreasing profiles, since much of the CO reaction product resides in dendrites (Wong-Riley, Trusk, Tripathi & Hoppe, 1989; Geyer, Malach & Sagi, 1991). Consider the over-simplified case of blobs containing only one type of neuron, with darkly-staining mitochondria. Even if these neurons were packed uniformly into a discrete area, the density profile would still show a gradual decrease. This is due to the distribution of overlapping dendritic arbors: their density would be greatest in the center, and would slowly decrease as one moves into the blob periphery. On the other hand, our observation of a decreasing density function could reflect a gradual change in the neuronal population from darkly staining to those with little CO activity. This situation appears to be reflected by the physiology of the cells in the blobs. The fact that there is nothing special about the blob "borders" is consistent with the anatomical observations of Malach (1992), who found that dendritic branches almost never respect the transition zone between a blob and the interblob region.

Magno/parvocellular influence on the upper cortical layers

It would be overly simplistic to assume that the determination of receptive fields in the cortex is solely a function of the relative amounts of magnocellular and parvocellular afferent inputs. Clearly, visual information undergoes a significant transformation between the lateral geniculate and the striate cortical output. Cortical receptive fields are highly selective for spatial frequency

and orientation, in comparison with their geniculate inputs (Maffei & Fiorentini, 1973; De Valois et al., 1975, 1982a; Schiller et al., 1976; Movshon et al., 1978a). Novel receptive field characteristics such as side- and end-inhibition are seen first in the striate cortex (Hubel & Wiesel, 1962; De Valois et al., 1985; Born & Tootell, 1991b). Cortical cells also exhibit a contrast adaptation not seen in geniculate cells (Maffei, Fiorentini & Bisti, 1973; Movshon & Lennie, 1979; Ohzawa, Sclar & Freeman, 1985; Bonds, 1991). It is apparent that intracortical interactions play a role in the organization of cortical receptive fields (Bishop, Coombs & Henry, 1973; Morrone, Burr & Maffei, 1982; De Valois & Tootell, 1983; Bonds, 1989).

At the same time, geniculate inputs do influence the nature of cortical receptive fields, and by examining these receptive fields, some inference can be drawn about the inputs. For example, Hawken and Parker (1984) showed the contrast sensitivity of cells in layer 4Cα to be higher than that of cells in 4Cβ, consistent with the contrast sensitivity difference in their geniculate afferents.

We therefore model in Fig. 19 the indirect magno- and parvocellular inputs into the superficial layers of striate cortex based upon the receptive field properties of cells in these layers (Edwards & Kaplan, 1990). This view maintains that indirect magnocellular input (i.e. input from layers 4Cα and 4B) is focused on the blobs, whereas parvocellular input is spread fairly uniformly throughout. This model is supported by the anatomical results of Lachica et al. (1992), although it postulates a non-discrete indirect input from the magnocellular pathway, rather than a tightly-focused, all-or-none input pattern. The model depends on our contrast sensitivity data. Indirect magnocellular inputs would confer high contrast sensitivity on cells near blob centers; indirect parvocellular inputs would result in cells with low contrast sensitivity distributed fairly evenly through layers 2/3.

The optimal spatial frequency data can be interpreted in two ways. On the one hand, since cells with low optimal spatial frequency are found throughout layers 2/3, and cells with high optimal spatial frequency are found within interblob regions, one might infer a diffuse indirect magnocellular input and a blob-sparing indirect
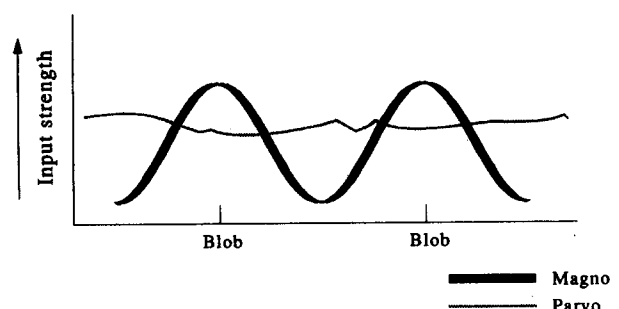

FIGURE 19. Model of indirect geniculate inputs to layers 2/3 of striate cortex. Magnocellular indirect inputs are focused on blobs, decreasing gradually from blob centers outward. Parvocellular inputs are spread diffusely throughout layers 2/3.

parvocellular input to the supragranular layers of the striate cortex. Note that this interpretation is at odds with the model set forth in Fig. 19, and is an unlikely explanation, since (1) it is not possible to reconcile this interpretation with accumulating anatomical data (Lund, 1973; Blasdel et al., 1985); (2) the absence of indirect parvocellular input to the blobs would preclude the formation of color-opponent receptive fields (Livingstone & Hubel, 1984; Ts'o & Gilbert, 1988); and (3) this interpretation is also inconsistent with our contrast sensitivity results. On the other hand, the notion of an indirect parvocellular input throughout layers 2/3 with a segregation of the *types* of parvocellular inputs between blobs and interblob regions, reconciles our contrast sensitivity and optimal spatial frequency data with other results. The parvocellular input near blob centers could consist primarily of type II cells (Wiesel & Hubel, 1966), with input from types I and III increasing toward the interblob regions. Since type II cells are larger and their center and surround regions have similar sizes, one might expect the optimal spatial frequency to be lower. This interpretation is more consistent with anatomical findings (Lachica et al., 1992), and allows color information to be processed within the blobs. Ts'o and Gilbert (1988) report cells of all response types (I–IV) in the blobs. However, in their study, cells were assigned in a binary fashion to blob or non-blob regions without regard for the graded nature of CO staining. This binary assignment results in a lumping of cell types that may actually be segregated with respect to CO density or distance from blob center.

Summation of parvocellular inputs could, in principle, be responsible for the receptive field properties of the cortical neurons we studied (Derrington & Lennie, 1984; Merigan & Eskin, 1986; but see Kaplan et al., 1990). In this case neurons would acquire high contrast sensitivity by summing several parvocellular afferents. For this to predict the contrast data, however, summation rules would necessarily differ between blob and interblob regions, since we did not find highly sensitive cells in the interblob regions. Receptive fields with preference for low spatial frequencies could be generated by the summation of parvocellular units with spatially displaced receptive fields. Here again, however, different summation rules would be required for blobs and interblobs.

Exclusive or mixed inputs?

Our data are consistent with the notion of focused magnocellular influence on the blobs, and diffuse parvocellular influence throughout layers 2/3. What might be
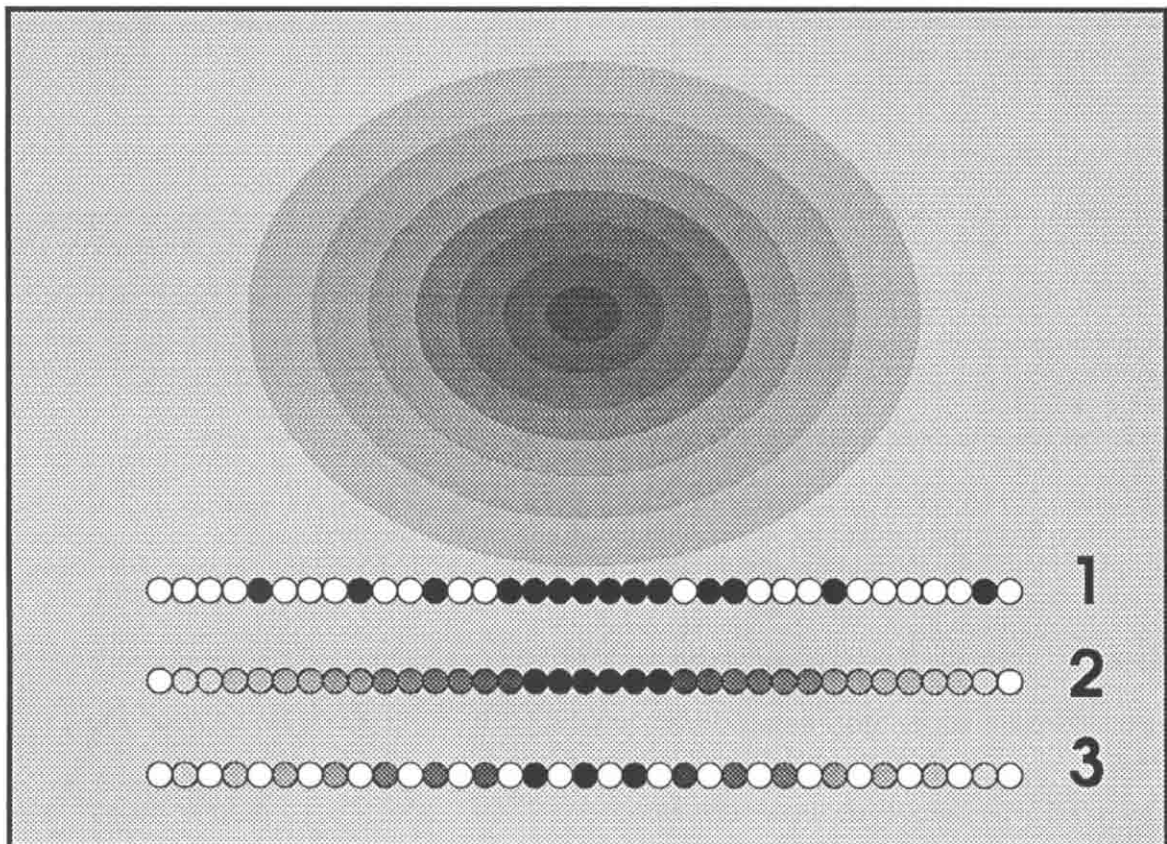

FIGURE 20. Possible magnocellular (black) and parvocellular (white) contributions to individual neurons. Each line of dots represents a row of neurons cutting across blob center. (1) Individual neurons receive exclusive magnocellular or parvocellular input. Indirect magnocellular input is biased towards blob centers. (2) Individual neurons receive a combination of magnocellular and parvocellular input. Magnocellular input to blob centers, changing to parvocellular input to interblobs. (3) Individual neurons receive combination of magnocellular and parvocellular input. Parvocellular input throughout, magnocellular input biased towards blob centers.

happening at the level of individual neurons? Do they receive exclusive magnocellular or parvocellular influence, or a weighted combination of both?

Consider the possibility that individual neurons are influenced exclusively by either magnocellular or parvocellular input, but not by both (Fig. 20, model 1). No mixing of pathways would occur on the level of single cells. This scheme would produce distinct neuronal populations, one with low and one with high contrast sensitivities.

A second possibility is that individual neurons receive a weighted combination of indirect inputs from both pathways (models 2 and 3 in Fig. 20). Perhaps neurons in the superficial layers simply integrate the afferent inputs along their dendritic spread, regardless of the nature of the inputs. In this case the gain of a cortical cell could be determined by the proportions of magnocellular and parvocellular indirect inputs. Model 2 shows the result of input integration over a large spatial extent. This model is inconsistent with our physiological data (Fig. 12). However, if the integration area of cortical neurons were decreased, local anisotropies in the indirect input patterns of both pathways would result in some blob cells not receiving strong magnocellular influence. This situation is depicted in model 3, and is most consistent with our data, since it accounts for the two major features of Fig. 12: (1) that there are cells with low sensitivity distributed throughout; and (2) that there is a *gradual* fall-off of contrast sensitivities from blob centers outward. As we reported here, the decrease in CO density with distance from blob centers is gradual as well. In addition to contrast sensitivity, the optimal spatial frequency and spatial resolution (Figs 15–18) also show a gradual change with distance from blob centers outward. Independent of the issue of magno- and parvocellular input, this gradual change in physiological properties could reflect the gradual change in CO density.

We should also consider the role that the direct input from the intercalated LGN layers might play in cortical organization and function. Since the physiological properties and input to these LGN cells are still unknown, their contribution to cortical processing remains obscure so far.

Distance vs density

A major objective of the current study was the determination of the relationship between CO density and the physiological properties of the cells in the cortex, in order to better understand the functional significance of the blob/interblob distinction. To our surprise we found that *distance* from blob center correlated better with the physiological parameters in our study than did the CO density itself. It is difficult to explain this observation. An opposite finding (that CO density is better correlated with the physiology than geometric distance) would have been easily explained on the basis of irregular or elliptical blob shapes, which would have added noise to the metric of distance. If CO density is not an epiphenomenon, irrelevant to neuronal function, then it is reasonable to conclude that the cortex contains a variety

of cell populations, and that CO density might be strongly related to the physiological properties of only *some* of them. Recording from a sample derived from several heterogeneous populations could easily obscure the relationship between CO density and physiological properties. It is also possible that CO is related to some other physiological parameter which we did not investigate. Furthermore, the underlying capillary bed, which is denser under the CO blobs (Zheng et al., 1991), might influence the physiological parameters we studied more than the CO density itself.

Functional implications

It appears that the physiological and anatomical distinctions between blobs and interblobs are not clear-cut, and accumulating data from several laboratories suggest that any clear functional distinction between the two regions is difficult to ascertain. It has been previously suggested (Livingstone & Hubel, 1987; Allman & Zucker, 1990) that blobs are particularly suited for the determination of luminance contrast, color contrast, and surface texture variables, whereas interblobs are devoted to form analysis, coding for contours and zero-crossings in the image. The validity of many of these distinctions has been challenged by further data: color-opponent cells have been found in interblobs as well as blobs (Ts'o & Gilbert, 1988; Lennie, Krauskopf & Sclar, 1990; Leventhal, Thompson, Liu, Neuman & Ault, 1993). Cells that encode higher-order texture interactions have been found throughout layers 2/3 (K. Purpura, unpublished observations). Our data argue that if interblob cells are indeed responsible for form analysis, this function will be greatly impaired at low contrasts, due to the low contrast sensitivity of interblob cells.

Our study, taken together with other available data, indicates that the encoding of contrast and spatial frequency does change as one moves away from the blobs. Cells far from blob centers do not respond reliably to contrasts below 8–12%, whereas blobs contain cells with a wide range of contrast detection thresholds. Allman and Zucker (1990) predicted that single blob cells are able to code a wide range of contrasts because their dynamic range stretches over several log units. While our data show a trend towards larger dynamic ranges for cells in the blobs, this trend is not significant. However, individual cells do not necessarily have to code the entire range of contrasts. It is possible that the coding is accomplished by an ensemble of cells, each operating over a different contrast range. Our data are consistent with the ensemble coding hypothesis, especially since we have found that blob cells have contrast thresholds which cover a wide range. Therefore, it appears that blobs are better equipped to signal the contrast of a stimulus than are interblobs.

In conclusion, cells near the blob centers appear to be concerned with the detection of patterns with a wide range of contrasts, whereas interblob neurons require fairly high contrasts to respond reliably. A wide range of spatial frequencies are coded by interblob cells, and the range narrows near blob centers. These blob/interblob

changes are gradual: the map of these properties in the cortex appears to be a continuum, consistent with the slow changes in CO density. The contrast data suggest the notion of focused magnocellular input to the blobs. Further physiological and psychophysical work will be needed to deepen our understanding of this intricate architectural feature, and of its relationship to parallel processing in the visual system.

REFERENCES

Albrecht, D. G. & Hamilton, D. B. (1982). Striate cortex of monkey and cat: Contrast response function. *Journal of Neurophysiology, 48,* 217–237.

Allman, J. M. & Zucker, S. (1990). Cytochrome oxidase and functional coding in primate striate cortex: A hypothesis. *Cold Spring Harbor Symposia on Quantitative Biology, 55,* 979–982.

Baizer, J. S., Ungerleider, L. G. & Desimone, R. (1991). Organization of visual inputs to the inferior temporal and posterior parietal cortex in macaques. *Journal of Neuroscience, 11,* 168–190.

Bishop, P. O., Coombs, J. S. & Henry, G. H. (1973). Receptive fields of simple cells in the cat striate cortex. *Journal of Physiology, London, 231,* 31–60.

Blakemore, C. & Vital-Durand, F. (1986). Organization and post-natal development of the monkey's lateral geniculate nucleus. *Journal of Physiology, London, 380,* 453–491.

Blasdel, G. G. & Fitzpatrick, D. (1984). Physiological organization of layer 4 in the macaque striate cortex. *Journal of Neuroscience, 4,* 880–895.

Blasdel, G. G., Lund, J. S. & Fitzpatrick, D. (1985). Intrinsic connections of macaque striate cortex: Axonal projections of cells outside lamina 4C. *Journal of Neuroscience, 5,* 3350–3369.

Blümcke, I., Hof, P. R., Morrison, J. H. & Celio, M. R. (1990). Distribution of parvalbumin immunoreactivity in the visual cortex of Old World monkeys and humans. *Journal of Comparative Neurology, 301,* 417–432.

Bonds, A. B. (1989). Role of inhibition in the specification of orientation selectivity of cells in the cat striate cortex. *Visual Neuroscience, 2,* 41–55.

Bonds, A. B. (1991). Temporal dynamics of contrast gain in single cells of the cat striate cortex. *Visual Neuroscience, 6,* 239–255.

Born, R. T. & Tootell, R. B. (1991a). Spatial frequency tuning of single units in macaque supragranular striate cortex. *Proceedings of the National Academy of Sciences, U.S.A., 88,* 7066–7070.

Born, R. T. & Tootell, R. B. (1991b). Single-unit and 2-deoxyglucose studies of side inhibition in macaque striate cortex. *Proceedings of the National Academy of Sciences, U.S.A., 88,* 7071–7075.

Britten, K. H., Shadlen, M. N., Newsome, W. T. & Movshon, J. A. (1992). The analysis of visual motion: A comparison of neuronal and psychophysical performance. *Journal of Neuroscience, 12,* 4745–4765.

Burkhalter, A., Felleman, D. J., Newsome, W. T. & Van Essen, D. C. (1986). Anatomical and physiological asymmetries related to visual areas V3 and VP in macaque extrastriate cortex. *Vision Research, 26,* 63–80.

Caceci, M. S. & Cacheris, W. P. (1984). Fitting curves to data. The Simplex algorithm is the answer. *Byte,* 340–362.

Croner, L. J., Purpura, K. & Kaplan, E. (1993). Response variability in retinal ganglion cells of primates. *Proceedings of the National Academy of Sciences, U.S.A., 90,* 8128–8130.

Crook, J. M., Lee, B. B., Tigwell, D. A. & Valberg, A. (1987). Thresholds to chromatic spots of cells in the macaque geniculate nucleus as compared to detection sensitivity in man. *Journal of Physiology, London, 392,* 193–211.

Derrington, A. M. & Lennie, P. (1984). Spatial and temporal contrast sensitivities of neurones in lateral geniculate nucleus of macaque. *Journal of Physiology, London, 357,* 219–240.

De Valois, K. & Tootell, R. B. (1983). Spatial-frequency-specific inhibition in cat striate cortex cells. *Journal of Physiology, London, 336,* 359–376.

De Valois, R. L., Albrecht, D. G. & Thorell, L. G. (1982a). Spatial frequency selectivity of cells in macaque visual cortex. *Vision Research, 22,* 545–559.

De Valois, R. L., Thorell, L. G. & Albrecht, D. G. (1985). Periodicity of striate-cortex-cell receptive fields. *Journal of the Optical Society of America A, 2,* 1115–1123.

De Valois, R. L., Yund, E. W. & Hepler, N. (1982b). The orientation and direction selectivity of cells in macaque visual cortex. *Vision Research, 22,* 531–544.

De Valois, R. L., De Valois, K., Ready, J. & von Blanckensee, H. (1975). Spatial frequency tuning of macaque striate cortex cells. *Investigative Ophthalmology & Visual Science, 15,* 16.

DeYoe, E. A. & Van Essen, D. C. (1985). Segregation of efferent connections and receptive field properties in visual area V2 of the macaque. *Nature, 317,* 58–61.

Edwards, D. P. & Kaplan, E. (1990). Contrast detection by primate cortical cells in and around the cytochrome oxidase blobs. *Investigative Ophthalmology & Visual Science (Suppl.), 31,* 88.

Fitzpatrick, D., Itoh, K. & Diamond, I. T. (1983). The laminar organization of the lateral geniculate body and the striate cortex in the squirrel monkey (*Saimiri sciureus*). *Journal of Neuroscience, 3,* 673–702.

Fries, W. (1986). Distribution of Meynert cells in primate striate cortex. Spatial relationships with cytochrome oxidase blobs. *Naturwissenschaften, 73,* 557–558.

Geyer, O., Malach, R. & Sagi, D. (1991). Direct demonstration of the relationship between cytochrome oxidase (CO) dense blobs and dendritic arbors in monkey striate cortex. *Investigative Ophthalmology & Visual Science, 32,* 1116.

Green, D. M. & Swets, J. A. (1966). *Signal detection theory and psychophysics.* New York: Wiley.

Hawken, M. J. & Parker, A. J. (1984). Contrast sensitivity and orientation selectivity in lamina IV of the striate cortex of Old World monkeys. *Experimental Brain Research, 54,* 367–372.

Hendrickson, A. E., Hunt, S. P. & Wu, J. Y. (1981). Immunocytochemical localization of glutamic-acid decarboxylase in monkey striate cortex. *Nature, 292,* 605–607.

Hendrickson, A. E., Wilson, J. R. & Ogren, M. P. (1978). The neuroanatomical organization of pathways between dorsal lateral geniculate nucleus and visual cortex in Old and New World primates. *Journal of Comparative Neurology, 183,* 123–136.

Hendry, S. H. C. & Yoshioka, T. (1994). A neurochemically distinct third channel in the macaque dorsal lateral geniculate nucleus. *Science, 264,* 575–577.

Hicks, T. P., Lee, B. B. & Vidyasagar, T. R. (1983). The responses of cells in macaque lateral geniculate nucleus to sinusoidal gratings. *Journal of Physiology, London, 337,* 183–200.

Horton, J. C. (1984). Cytochrome oxidase patches: A new cytoarchitectonic feature of monkey visual cortex. *Philosophical Transactions of the Royal Society of London B, 304,* 199–253.

Horton, J. C. & Hubel, D. H. (1981). Regular patchy distribution of cytochrome oxidase staining in primary visual cortex of macaque monkey. *Nature, 292,* 762–764.

Hubel, D. H. & Livingstone, M. S. (1987). Segregation of form, color, and stereopsis in primate area 18. *Journal of Neuroscience, 7,* 3378–3415.

Hubel, D. H. & Livingstone, M. S. (1990). Color and contrast sensitivity in the lateral geniculate body and primary visual cortex of the macaque monkey. *Journal of Neuroscience, 10,* 2223–2237.

Hubel, D. H. & Wiesel, T. N. (1962). Receptive fields, binocular interaction and functional architecture in the cat's visual cortex. *Journal of Physiology, London, 160,* 106–154.

Hubel, D. H. & Wiesel, T. N. (1965). Receptive field and functional architecture in two nonstriate visual areas (18–19) of the cat. *Journal of Neurophysiology, 28,* 229–289.

Hubel, D. H. & Wiesel, T. N. (1972). Laminar and columnar distribution of geniculo-cortical fibers in the macaque monkey. *Journal of Comparative Neurology, 146,* 421–450.

Kaplan, E. & Shapley, R. M. (1982). X and Y cells in the lateral geniculate nucleus of macaque monkeys. *Journal of Physiology, London, 330,* 125–143.

Kaplan, E. & Shapley, R. M. (1986). The primate retina contains two types of ganglion cells, with high and low contrast sensitivity. *Proceedings of the National Academy of Sciences, U.S.A., 83*, 2755–2757.

Kaplan, E., Lee, B. B. & Shapley, R. M. (1990). New views of primate retinal function. *Progress in Retinal Research, 9*, 273–336.

Kuljis, R. O. & Rakic, P. (1989). Neuropeptide Y-containing neurons are situated predominantly outside cytochrome oxidase puffs in macaque visual cortex. *Visual Neuroscience, 2*, 57–62.

Lachica, E. A., Beck, P. D. & Casagrande, V. A. (1992). Parallel pathways in macaque monkey striate cortex: Anatomically defined columns in layer III. *Proceedings of the National Academy of Sciences, U.S.A., 89*, 3566–3570.

Lennie, P., Krauskopf, J. & Sclar, G. (1990). Chromatic mechanisms in striate cortex of macaque. *Journal of Neuroscience, 10*, 649–669.

LeVay, S. & Nelson, S. B. (1991). Columnar organization of the visual cortex. In Leventhal, A. G. (Ed.), *Vision and visual dysfunction (the neural basis of visual function)* (pp. 266–315). London: Macmillan.

Leventhal, A. G., Thompson, K. G., Liu, D., Neuman, L. M. & Ault, S. J. (1993). Form and color are not segregated in monkey striate cortex. *Investigative Ophthalmology & Visual Science (Suppl.), 34*, 555.

Livingstone, M. S. & Hubel, D. H. (1984). Anatomy and physiology of a color system in the primate visual cortex. *Journal of Neuroscience, 4*, 309–356.

Livingstone, M. S. & Hubel, D. H. (1987). Psychophysical evidence for separate channels for the perception of form, color, movement, and depth. *Journal of Neuroscience, 7*, 3416–3468.

Livingstone, M. S. & Hubel, D. H. (1988). Segregation of form, color, movement, and depth: Anatomy, physiology, and perception. *Science, 240*, 740–749.

Lund, J. S. (1973). Organization of neurons in the visual cortex, area 17, of the monkey (*Macaca mulatta*). *Journal of Comparative Neurology, 147*, 455–496.

Lund, J. S. & Boothe, R. G. (1975). Interlaminar connections and pyramidal neuron organisation in the visual cortex, area 17, of the macaque monkey. *Journal of Comparative Neurology, 159*, 305–334.

Maffei, L. & Fiorentini, A. (1973). The visual cortex as a spatial frequency analyser. *Vision Research, 13*, 1255–1267.

Maffei, L., Fiorentini, A. & Bisti, S. (1973). Neural correlate of perceptual adaptation to gratings. *Science, 182*, 1036–1038.

Malach, R. (1992). Dendritic sampling across processing streams in monkey striate cortex. *Journal of Comparative Neurology, 315*, 303–312.

Maunsell, J. H. R. & Van Essen, D. C. (1983). The connections of the middle temporal visual area (MT) and their relationship to a cortical hierarchy in the macaque monkey. *Journal of Neuroscience, 3*, 2563–2586.

Merigan, W. H. & Eskin, T. A. (1986). Spatio-temporal vision of macaques with severe loss of P_β retinal ganglion cells. *Vision Research, 26*, 1751–1761.

Merrill, E. G. & Ainsworth, A. (1972). Glass-coated platinum-plated tungsten microelectrodes. *Medical & Biological Engineering, 10*, 662–672.

Milkman, N., Schick, G., Rossetto, M., Ratliff, F., Shapley, R. & Victor, J. (1980). A two-dimensional computer-controlled visual stimulator. *Behavior Research Methods and Instrumentation, 12*, 283–292.

Morel, A. & Bullier, J. (1990). Anatomical segregation of two cortical visual pathways in the macaque monkey. *Visual Neuroscience, 4*, 555–578.

Morrone, M. C., Burr, D. C. & Maffei, L. (1982). Functional implications of cross-orientation inhibition of cortical visual cells. I. Neurophysiological evidence. *Proceedings of the Royal Society of London B, 216*, 335–354.

Movshon, J. A. & Lennie, P. (1979). Pattern-selective adaptation in visual cortical neurones. *Nature, 278*, 850–852.

Movshon, J. A., Thompson, I. D. & Tolhurst, D. J. (1978a). Spatial and temporal contrast sensitivity of neurones in areas 17 and 18 of the cat's visual cortex. *Journal of Physiology, London, 283*, 101–120.

Movshon, J. A., Thompson, I. D. & Tolhurst, D. J. (1978b). Spatial summation in the receptive fields of simple cells in the cat's striate cortex. *Journal of Physiology, London, 283*, 53–77.

Ohzawa, I., Sclar, G. & Freeman, R. D. (1985). Contrast gain control in the cat's visual system. *Journal of Neurophysiology, 54*, 651–667.

Payne, B. R. & Peters, A. (1989). Cytochrome oxidase patches and Meynert cells in monkey visual cortex. *Neuroscience, 28*, 353–363.

Purpura, K. P., Kaplan, E. & Shapley, R. M. (1989). Fluctuations in spontaneous discharge and visual responses in M and P pathways of the macaque monkey. *Investigative Ophthalmology & Visual Science (Suppl.), 30*, 297.

Schiller, P. H., Finlay, B. L. & Volman, S. F. (1976). Quantitative studies of single-cell properties in monkey striate cortex: III. Spatial frequency. *Journal of Neurophysiology, 39*, 1334–1351.

Shapley, R., Kaplan, E., & Soodak, R. (1981). Spatial summation and contrast sensitivity of X and Y cells in the lateral geniculate nucleus of the macaque. *Nature, 292*, 543–545.

Shipp, S. & Zeki, S. (1985). Segregation of pathways leading from area V2 to areas V4 and V5 of macaque monkey visual cortex. *Nature, 315*, 322–325.

Silverman, M. S., Grosof, D. H., De Valois, R. L. & Elfar, S. D. (1989). Spatial-frequency organization in primate striate cortex. *Proceedings of the National Academy of Sciences, U.S.A., 86*, 711–715.

Skottun, B. C., De Valois, R. L., Grosof, D. H., Movshon, J. A., Albrecht, D. G. & Bonds, A. B. (1991). Classifying simple and complex cells on the basis of response modulation. *Vision Research, 31*, 1079–1086.

Spitzer, H. & Hochstein, S. (1985). Simple- and complex-cell response dependences on stimulation parameters. *Journal of Neurophysiology, 53*, 1244–1265.

Tolhurst, D. J., Movshon, J. A. & Dean, A. F. (1983). The statistical reliability of signals in single neurons in cat and monkey visual cortex. *Vision Research, 23*, 775–785.

Tootell, R. B. H., Hamilton, S. L. & Switkes, E. (1988a). Functional anatomy of macaque striate cortex: IV. Contrast and magno-parvo streams. *Journal of Neuroscience, 8*, 1594–1609.

Tootell, R. B. H., Silverman, M. S., Hamilton, S. L., Switkes, E. & De Valois, R. L. (1988b). Functional anatomy of macaque striate cortex. V. Spatial frequency. *Journal of Neuroscience, 8*, 1610–1624.

Trusk, T. C., Kaboord, W. S. & Wong-Riley, M. T. T. (1990). Effects of monocular enucleation, tetrodotoxin, and lid suture on cytochrome-oxidase reactivity in supragranular puffs of adult macaque striate cortex. *Visual Neuroscience, 4*, 185–204.

Ts'o, D. Y. & Gilbert, C. D. (1988). The organization of chromatic and spatial interactions in the primate striate cortex. *Journal of Neuroscience, 8*, 1712–1727.

Ungerleider, L. G. & Desimone, R. (1986a). Cortical connections of visual area MT in the macaque. *Journal of Comparative Neurology, 248*, 190–222.

Ungerleider, L. G. & Desimone, R. (1986b). Projections to the superior temporal sulcus from the central and peripheral field representations of V1 and V2. *Journal of Comparative Neurology, 248*, 147–163.

Ungerleider, L. G. & Mishkin, M. (1982). Two cortical visual systems. In Ingle, D. J., Goodale, M. A. & Mansfield, R. J. W. (Eds), *Analysis of visual behavior* (pp. 549–586). Cambridge, Mass.: MIT Press.

Wiesel, T. N. & Hubel, D. H. (1966). Spatial and chromatic interactions in the lateral geniculate body of the rhesus monkey. *Journal of Neurophysiology, 29*, 1115–1156.

Wong-Riley, M. T. T. & Carroll, E. W. (1984). Effect of impulse blockage on cytochrome oxidase activity in monkey visual system. *Nature, 307*, 262–264.

Wong-Riley, M. T. T., Trusk, T. C., Tripathi, S. C. & Hoppe, D. A. (1989). Effect of retinal impulse blockage on cytochrome oxidase-rich zones in the macaque striate cortex: II. Quantitative electron-microscopic (EM) analysis of neuropil. *Visual Neuroscience, 2*, 499–514.

Woolsey, T. A. & van der Loos, H. (1970). The structural organization of layer IV in the somatosensory region (SI) of mouse cerebral cortex. The description of a cortical field composed of discrete cytoarchitectonic units. *Brain Research, 17*, 205–242.

Zheng, D., LaMantia, A.-S. & Purves, D. (1991). Specialized vascularization of the primate visual cortex. *Journal of Neuroscience, 11*, 2622–2629.